Cyclic compressive behavior and load-strain model of FRP-ECC-HSC composite columns

Shuai Li, Aff.M.ASCE[1]; Tak-Ming Chan, M.ASCE[2]; Ben Young, F.ASCE[3]

[1]Postdoctoral Fellow, Dept. of Civil and Environmental Engineering, Hong Kong Polytechnic Univ., Hong Kong, China.

[2]Associate Professor, Dept. of Civil and Environmental Engineering, Hong Kong Polytechnic Univ., Hong Kong, China (corresponding author). ORCID: https://orcid.org/0000-0003-0478-2305. Email: tak-ming.chan@polyu.edu.hk

[3]Professor, Dept. of Civil and Environmental Engineering, Hong Kong Polytechnic Univ., Hong Kong, China.

Abstract

An innovative composite column, which consists of high strength concrete (HSC) core, engineered cementitious composites (ECC) ring and fiber-reinforced polymer (FRP) tube, has been developed and tested subjected to monotonic axial compression by the authors recently. In this study, cyclic compressive behavior of this proposed FRP-ECC-HSC composite column was examined. Test parameters including HSC core strength, FRP tube thickness and ECC ring thickness were investigated. Typical failure modes, dilation behavior and axial load versus axial strain behavior were discussed and analyzed. It is found that the FRP-ECC-HSC composite columns could exhibit improved deformability compared with the counterpart traditional FRP-confined HSC columns, with the ultimate axial compressive strain increased by 0.7-69.1% for the tested specimens. Meanwhile, the ultimate axial strain for cyclically loaded specimens is larger than that for monotonically loaded specimens in general, indicating a delayed column failure. Cyclic axial load-axial strain models, including the envelope model, unloading and reloading models, plastic strain equation and stress deterioration equation, were proposed to predict the cyclic compressive behavior of the tested specimens. The proposed model was verified with the test results and exhibited good performance.

Author keywords: Confinement; Cyclic compression; Cyclic load-strain model; FRP-ECC-HSC composite column; Hoop strain; Ultimate axial strain

Introduction

Fiber-reinforced polymer (FRP) confined concrete column is an effective structural form with the significantly improved compressive strength and strain of concrete under lateral confinement provided by FRP (Ozbakkaloglu, et al., 2013; Zhu et al., 2020; Lai et al., 2020). However, FRP confining efficiency can be reduced with the increase of compressive strength of concrete (Pessiki et al., 2001; Wu and Jiang, 2013). The increased concrete brittleness may lead to premature failure of FRP-confined high strength concrete (HSC) columns and cause poor ductility (Pour et al., 2018; Yang and Feng, 2021; Sirach et al., 2021). This brings an obstacle to a wider engineering application of HSC columns using FRP confinement, especially when the FRP-confined HSC columns cannot withstand the relatively large deformations under seismic loadings (Abdallah and El-Salakawy, 2022). Various FRP-steel-concrete composite columns have been developed in recent years to improve the confined concrete column performance utilizing the good ductility of steel (Zhang et al., 2021; Wei et al., 2022). Steel tubes and FRP tubes were used as the inner tubes and outer tubes to provide lateral confinement to the concrete and contribute to the load resistance in the composite columns, such as double-skin tubular columns (DSTCs) (Zhang et al., 2021) and double tube tubular columns (DTTCs) (Li and Zhao, 2020). Advanced theoretical models were also proposed to describe the stress-strain responses of concrete under the dual confinements of FRP and steel.

An innovative composite column, which consists of high strength concrete (HSC) core, engineered cementitious composites (ECC) ring and fiber-reinforced polymer (FRP) tube, was developed by the authors recently as shown in Fig. 1. ECC is a cementitious material reinforced with short fibers and can develop good ductility performance with the tensile strain capacity of 1%-8% (Li et al., 2001, Xu et al., 2022). The fiber bridging effect will prevent the width of a single crack from growing continuously and lead to the generation of multiple fine cracks with limited width. In recent research, the use of ECC has been explored in various structural members and exhibited improved performance (Li et al., 2019; Lee et al., 2020; Nguyen and Lee, 2021). Dang et al. (2020) and Yuan et al. (2021) tested the compressive responses of ECC stub columns under FRP confinement and reported that FRP-confined ECC could exhibit slower lateral dilation and larger axial compressive strain at FRP rupture compared to FRP-confined normal concrete with similar compressive strength under the similar FRP confinement. Li et al. (2022a) investigated the structural behavior of GFRP-concrete double tube composite column, in which an additional pultruded FRP tube was added between the ring concrete and core concrete compared with the FRP-ECC-HSC column in the current study. Both normal concrete and ECC with comparable compressive strengths were used in the ring for the double tube columns. It was noted that the columns having ECC ring could develop larger ultimate axial compressive strain and better deformability compared to the columns having normal concrete ring. In this study, ECC ring in this proposed FRP-ECC-HSC column is used to ease the HSC core brittleness and increase the deformability and ductility of the column. Compared with the aforementioned FRP-concrete-steel composite columns, the steel-free FRP-ECC-HSC column is without corrosion problems and also has the potential to be used in coastal areas and marine environments.

Understanding cyclic compressive performance of FRP-confined concrete is of vital importance to seismic retrofitting of various concrete columns. Extensive cyclic stress-strain models have been developed for predicting the hysteresis responses of FRP-confined concrete columns (Bai et al., 2021; Zhou et al., 2021; Zeng et al., 2021). Shao et al. (2006) proposed the first cyclic stress-strain model with limited test data. Lam et al. (2006) evaluated the model and found that it could not provide accurate predictions on the unloading path. Lam and Teng (2009) proposed a new model with more accurate descriptions of unloading and reloading cycles, plastic strain and stress deterioration. With the incorporation of FRP-confined HSC test data, Yu et al. (2015) proposed a modified cyclic model based on Lam and Teng's model (Lam and Teng, 2009). Wang et al. (2012) and Hany et al. (2015) extended the study of cyclic models to FRP-confined concrete with larger size and with non-circular sections. Li et al. (2018) considered the confinement rigidity in the equations of the proposed cyclic model, which could depict the cyclic compressive behavior including both softening and hardening in the post-peak stage. In recent years, with the development of FRP-concrete-steel columns, advanced cyclic models were further proposed with the considerations of combined effects of different components (Bai et al., 2017; Zhang et al., 2022).

In this study, axial compressive performance of the proposed FRP-ECC-HSC composite column was experimentally investigated, in which 9 specimens were loaded subjected to monotonic axial compression and firstly reported in Li et al. (2023) and 13 new specimens were loaded subjected to cyclic axial compression. Corresponding traditional FRP-confined HSC columns were prepared and investigated for comparisons as well. Typical failure modes, dilation behavior and axial load versus axial strain behavior were discussed and analyzed. Cyclic load-strain models, which were generated with the cyclic stress-strain models of HSC and ECC under FRP confinement, were proposed for predicting the cyclic compressive performance of the FRP-ECC-HSC columns.

Experimental investigation

Material properties

Concrete

Two grades of HSC, C70 and C90 with the mixtures provided in Table 1, were considered to form the HSC core in this study. Five 150 mm × 300 mm concrete cylinders were tested for C70 and C90 respectively, to get the compressive properties as shown in Table 2. The mixture design of ECC50, as presented in Table 1, was used to cast the ECC ring. 2% of polyethylene (PE) fiber (by volume), with fiber properties shown in Table 3, was adopted in the ECC mixture. ECC compressive properties were obtained with on five 75 mm × 150 mm cylinders through compression tests and presented in Table 2. The sizes of both HSC cylinders and ECC cylinders could meet the requirements of the test standards ASTM C192 (2019) and ASTM C31 (2019).

ECC tensile coupon tests were also conducted based on JSCE (2008) to obtain the direct tensile properties. Typical failure modes and tensile stress versus strain curves are shown in Fig. 2. Strain hardening behavior with ductile manner and multiple cracking are noted for the ECC coupons. The tensile strength and tensile strain capacity are 5.0 MPa and 3-4%, respectively.

FRP

Filament winding manufacturing process was used for the FRP tubes. The orientation of glass fibers is 80 degree with respective to the longitudinal axis. This can lead to a large hoop stiffness and provide lateral confinement on the inner concrete effectively. FRP tubes are with the nominal inner diameter of 200 mm. 7 layers (F7) and 10 layers (F10) of glass fiber were considered to form two different thicknesses of the FRP tube and generate different levels of confinement. Five FRP rings (50 mm for the height) were cut from the FRP tubes and examined through split-disk tests based on ASTM D2290-08 (2008) standard to get the tensile properties in the circumferential direction for F7 and F10, respectively. Another five FRP rings (60 mm for the height) were compressed according to GB/T5350 (2005) to get the compressive properties in the longitudinal direction. Test results for the FRP tubes are summarized in Table 4.

Test specimens

A total of 22 composite columns were included in the test program, in which 9 specimens were loaded subjected to monotonic axial compression and firstly reported in Li et al. (2023) and 13 new specimens were loaded subjected to cyclic axial compression. The nominal diameter and height of tested specimens are 200 mm and 400 mm, respectively. Two ECC thicknesses (15 mm and 25 mm), two HSC grades (C70 and C90) and two FRP thicknesses (F7 and F10) were considered. Specimen labels are presented in Table 5. "F7" or "F10" refers to the FRP tube having 7 or 10 layers of fiber, "H70" or "H90" stands for C70 or C90 used for the HSC core, and "E50" stands for ECC50 used for the ECC ring. "15" or "25" is the thickness of ECC ring being 15 mm or 25 mm. "M" or "C" stands for the monotonic or cyclic compression. For example, "F7-E50-H70-15-C" refers to the specimen with F7 as FRP tube, ECC50 as ECC ring with the thickness of 15 mm and C70 as HSC core under cyclic axial compression. Two identical cyclically loaded specimens were prepared for some cases and were marked as "C1" and "C2". Compression tests on traditional FRP-confined HSC columns were also carried out for comparisons. Fig. 3 shows the preparation process of FRP-ECC-HSC columns in the laboratory. HSC core was firstly cast and then placed in the center of FRP tube. ECC was finally cast into the region between HSC core and FRP tube to form the composite column. In engineering practice, ECC ring can be cast firstly, followed by FRP filament winding on the surface of the ECC ring to prefabricate the FRP-ECC tube in the factory, which can then be transported to construction sites to cast the HSC core. With this approach, the construction process of the composite column can be eased to save the cost of time and on-site labor. 20 mm-wide CFRP wrapping strips were used to strengthen two ends of the column. Gypsum capping was used to flatten the top and bottom column surfaces, to ensure that the specimen was fully contacting the loading plates and pure axial compression could be applied.

Test setup and loading

Figs. 4(a) and (b) show the test setup and specimen instrumentation for the compression test. Twelve hoop strain gauges and four axial strain gauges were attached on the FRP tube surface at the mid-height level to monitor hoop strains and axial strains, respectively. Four LVDTs were used to measure the axial displacement of the column between two ends. Axial loads, reading of strain gauges and LVDTs were simultaneously recorded through a data logger. Displacement control was used for the compression tests and the loading rate was 0.24 mm per minute. For monotonic compression, the axial load was stopped when FRP rupture occurred. For cyclic compression test, the loading scheme is presented in Fig. 4(c). Compressive loading was applied to the first target displacement, followed by the unloading process to approximate 0 kN to complete the first loading cycle. In the subsequent loading cycles, the corresponding target displacement was larger than the previous one and the difference was kept nearly constant. A pre-set program was adopted to control this loading/unloading procedure until column failure. The above loading scheme is adopted based on the literatures (Lam and Teng, 2009; Zhang et al., 2015; Zhou et al., 2021) in which the influence of loading and unloading cycles at different strain levels on the performance of concrete columns under FRP confinement was investigated.

Test results and discussions

Failure modes

Typical failure modes for tested specimens are presented in Fig. 5. FRP tube rupture in the circumferential direction governed the column failure as presented in Fig. 5(a). White patches of resin failure were observed firstly during the test before the FRP rupture. Cracking of concrete can be observed after removing the FRP tubes as shown in Fig. 5(b). Relatively large and localized cracks can be noticed for FRP-confined HSC columns, indicating the brittle shear failure. By contrast, FRP-ECC-HSC composite columns could generate multiple fine cracks on the ECC ring, which were uniformly distributed. Meanwhile, the cracks were slightly finer for the FRP-ECC-HSC columns with thicker ECC ring. Similar failure modes could be noted for the FRP-ECC-HSC specimens having different HSC core strengths and FRP tube thicknesses during the tests and from the failed specimens.

Besides the failure modes, the investigated test variables can also bring effects on the load and strain responses, which are further discussed in the following sections.

Axial load-axial strain responses

Fig. 6 show the axial load-axial strain curves of the specimens. Axial strains obtained from axial strain gauges and LVDTs agreed well with each other in the initial stage, while started to deviate at the plastic stage. Readings obtained from the four axial strain gauges would become different because of the non-uniform concrete cracking and damage after entering plastic stage and would be not accurate when white patches occurred at the strain gauge locations. Therefore, the axial strains calculated with the averaged displacements measured from the LVDT, which reflected the overall axial shortening behavior of the column, and the corresponding column heights were used in Fig. 6 and the discussions presented in this study.

All the specimens under monotonic loading exhibit the typical three-stage axial load-axial strain curves. A strain softening stage after the first peak load can be noted, followed by stress recovery till FRP rupture. For FRP-confined HSC specimens with tube thickness of F7, the ultimate load corresponding to FRP rupture is nearly the same as the first peak load as shown in Figs. 6(a) and (d). It indicates that the confinement is not strong enough to achieve an improved strength for the confined HSC. For specimens with F10 as the FRP tube, an enhanced ultimate load can be obtained compared to the first peak load as shown in Fig. 6(g). Comparing the columns having C90 HSC core as shown in Figs. 6(d-e) with the columns with C70 HSC core as shown in Figs. 6(a-c), the load drop during the strain softening period is relatively more obvious due to the higher HSC core brittleness. For FRP-ECC-HSC specimens as shown in Figs. 6(b,c,e,f,h,i), the load drop is less obvious and the strain hardening stage is more stable, compared to those of the counterpart FRP-confined HSC specimens. When ECC proportion increases, load resistance of the FRP-ECC-HSC composite column will decrease since the ECC ring strength is lower than HSC core strength. Compared with traditional FRP-confined HSC specimens, the ultimate axial compressive strain of FRP-ECC-HSC specimens can be effectively improved, and the improvement will be larger if the ECC proportion is larger, which demonstrates the enhanced deformability. Envelope curves for columns under cyclic compression are close to the axial load-strain curves for columns under monotonic compression as shown in Fig. 6, which agrees with the typical behavior of FRP-confined concrete reported in the literature (Lam et al., 2006; Yu et al., 2015; Dang et al., 2020; Li et al., 2022b). First peak load F_1, ultimate load F_{cu} and ultimate axial strain ε_{cu} corresponding to FRP rupture of the specimens are listed in Table 5. Cyclically loaded specimens could generally develop 0.7-25.5% larger ultimate axial compressive strain than the corresponding monotonically loaded specimens as presented in Table 5, except for the specimen F7-E50-H90-25-C2 that endured an earlier failure. It was reported in Lam et al. (2006) that the average FRP rupture strain could be improved for FRP-confined concrete under cyclic loading than the counterpart under monotonic loading. With the enhanced FRP rupture strain, the column failure could be delayed with enhanced ultimate compressive strength and ultimate axial strain. This behavior has also been observed by Dang et al. (2020) and Li et al. (2022b) for FRP-confined ECC stub columns. In the current study, the same reason is believed to be applicable to FRP-ECC-HSC columns.

Hoop strain-axial strain responses

Fig. 7 presents the hoop strain-axial strain relations for the tested columns. Axial compressive strains and hoop tensile strains are assigned with positive values and negative values, respectively. Similar to the load-strain curves, envelope curves for columns under cyclic loading are close to the hoop strain-axial strain curves for the counterpart monotonically compressed columns. Cyclically loaded columns have the larger ultimate axial strain and FRP hoop rupture strain compared to the corresponding monotonically loaded columns in general. Fig. 8 presents the comparisons of hoop strain-axial strain behavior. It can be noted that FRP-ECC-HSC specimens can generally exhibit a lower hoop strain than the counterpart FRP-confined HSC specimens under the same axial strain during the loading process for both monotonic and cyclic loadings, which reflects that FRP-ECC-HSC columns present a slower hoop strain development. This may be caused by the unique dilation behavior of ECC. Due to the effect of fiber bridging through the cracks, lateral dilation of FRP-confined ECC is restrained under compressive loads and will present a slower development of hoop strain compared with FRP-confined normal concrete (Dang et al., 2020; Yuan et al., 2021). With this slower development of hoop strain, the ultimate axial compressive strain will be consequently enhanced, considering the same FRP hoop rupture strain is reached. Compared Figs. 7(d-f) with Figs. 7(g-i), it can also be observed that the increase of hoop strain will be slower under the larger lateral confinement provided by the thicker FRP tube. If HSC core strength increases from C70 to C90, the ultimate axial compressive strain will decrease accordingly as observed in Figs. 7(a-c) and Figs. 7(d-f). Ultimate axial strains ε_{cu} and hoop rupture strains $\varepsilon_{h,rup}$ for the tested specimens are summarized in Table 5.

Hoop strain distributions

Typical hoop strain distributions for the tested columns are presented in Fig. 9. It is found that FRP-ECC-HSC specimens can generate more uniform hoop strain distributions than FRP-confined HSC specimens, comparing Figs. 9(c,e) with Fig. 9(a) for monotonic loading and comparing Figs. 9(d,f) with Fig. 9(b) for cyclic loading. Hoop strain distribution mechanisms for the two types of columns can be explained as presented in Fig. 10. When HSC generates localized large cracks due to its high brittleness, the FRP tube hoop strain at the corresponding locations will be increased as well (as shown in Fig. 10(a)). If the concentrated hoop strains reach the material ultimate tensile strain, FRP premature rupture will occur at these locations. Under this circumstance, the FRP tube will not be fully utilized since the strain level is still relatively lower at other locations. In the FRP-ECC-HSC composite column, ECC ring could generate multiple fine microcracks to re-distribute the concentrated hoop strain from inner HSC core to outer FRP tube. More uniform FRP strain distribution can be realized (as shown in Fig. 10(b)). Therefore, it mitigates the FRP premature rupture to yield an increased average FRP rupture strain. This full FRP utilization will also delay the overall column failure and result in the enhanced ultimate axial strain, which has been confirmed with the hoop strain-axial strain responses as shown in Fig. 7. This behavior mentioned above could also be proved by the ECC ring multiple cracking as shown in Fig. 5(b).

Hoop strain distributions are more uniform for the columns under cyclic compression (Figs. 9(b,d,f)) compared with those under monotonic compression (Figs. 9(a,c,e)). This phenomenon has also been reported previously (Lam et al., 2006; Dang et al., 2020). It is believed that cracks could be more uniformly distributed during the repeated loading and unloading cycles, in comparison to that the cracks may tend to be concentrated for specimens subjected to monotonic compression. Consequently, both the average hoop strain corresponding to FRP rupture and the ultimate axial compressive strain of cyclically compressed columns are relatively larger than those of monotonically compressed ones.

Cyclic load-strain models

Prediction of axial load

Load carrying capacity analysis of FRP-ECC-HSC composite columns is more complicated compared to that of the traditional FRP-confined concrete columns, because of the two concrete types involved in the core region and ring region. Fig. 11 shows the mechanism diagram of the FRP-ECC-HSC composite column. A_{hsc}, A_{ecc} and A_{frp} are the cross-sectional areas of HSC core, ECC ring and FRP tube, respectively. $f_{l,frp}$ is the FRP tube confining pressure, while $f_{l,hsc}$ is the confining pressure on the HSC core. Meanwhile, $f_{l,frp}$ and $f_{l,hsc}$ are equal to the lateral confining pressures applied on the outer and inner ECC ring. ECC ring could not generate extra lateral confinement on HSC core, because ECC is under tri-axial compression. Therefore, the lateral confining pressures applied on HSC core and ECC ring can be regarded as the same and both equal to that contributed by the FRP tube in the composite column. The confining pressure f_l is calculated as follows:

$$f_l = K_l \varepsilon_h = \frac{2E_f t_f \varepsilon_h}{D} \tag{1}$$

where E_f, t_f, D and ε_h are the hoop elastic modulus, thickness, inner diameter and hoop strain of the FRP tube; K_l is the confining stiffness. Eq. (1) is derived based on the linear elastic property of FRP and force equilibrium in the hoop direction of the circular concrete section under lateral FRP confinement and is widely used in the literature (Lam and Teng, 2003; Yang et al., 2021; Yuan et al., 2021). The lateral confining pressure f_{lu} at FRP rupture is calculated with the following equation by substituting the hoop strain with FRP hoop rupture strain:

$$f_{lu} = K_l \varepsilon_{h,rup} \tag{2}$$

in which $\varepsilon_{h,rup}$ is the actual FRP hoop rupture strain. The calculated f_{lu} are summarized in Table 5 for tested specimens.

Total axial load of the composite column is calculated by combining the corresponding axial loads carried by different portions, which is an approach widely adopted for composite columns under compressive loadings (Zhang et al., 2017; Zhang et al., 2021; Li et al., 2022a). The recommended expression is shown as follows:

$$F = A_{hsc}\sigma_{c,hsc} + A_{ecc}\sigma_{c,ecc} + A_{frp}\sigma_{c,frp} \tag{3}$$

in which $\sigma_{c,hsc}$ and $\sigma_{c,ecc}$ are the confined compressive stresses of HSC core and ECC ring; $\sigma_{c,frp}$ is the compressive stress of FRP tube. FRP tube stress can be determined through the compressive stress-strain relation obtained by the material tests (FRP ring compression tests). The ultimate compressive strain corresponding to FRP ring failure obtained from the material tests is lower than the ultimate axial compressive strain of the FRP-ECC-HSC column corresponding to FRP hoop rupture. Since FRP tube is fully supported by the inner concrete in the composite column, it is assumed that the FRP tube compressive strength is unchanged after reaching the compressive strain corresponding to FRP ring failure obtained from the material tests till the column failure by FRP hoop rupture. Meanwhile, the axial load contributed by the FRP tube is quite limited, and only counts 3.5% - 6.2% of the total load carried by the composite column for all the tested specimens according to the calculation with the obtained test results in the current study. The assumption that the compressive strength of FRP tube can be considered to be unchanged after reaching its ultimate compressive strain till composite column failure by FRP hoop rupture has also been widely adopted by the existing literatures for FRP tube confined concrete (Zhang et al., 2015; Zhang et al., 2017; Zhang et al., 2021; Zhou et al., 2021; Xie et al., 2022) to simplify the design equations, which will not cause any significant effects. The confined compressive strength of HSC and ECC can be determined by the stress-strain models, as presented in the following sections.

Cyclic stress-strain model and terminology

For FRP-confined concrete, typical cyclic stress-strain model is composed of the envelope curve, unloading and reloading paths as shown in Fig. 12. The envelope curve is regarded as the upper boundary of the cyclic curves. In the unloading path as shown in segment AB in Fig. 12, axial stress would reduce when axial strain increases. Axial strain ε_{un} and axial stress σ_{un} at the unloading point

A are defined as the unloading strain and unloading stress, respectively. When stress in the unloading curve becomes zero at point B, the corresponding strain is termed as plastic strain ε_{pl}. Reloading path starts at point B with the increase of axial stress and strain and meets the envelope curve at point D ($\varepsilon_{ret,env}, \sigma_{ret,env}$). At reference point C in the reloading curve, the axial strain ε_{ref} equals to the unloading strain ε_{un}. The corresponding stress σ_{new} at point C is lower than the unloading stress σ_{un} at point A, which reflects the stress deterioration behavior. The envelope curve, unloading curve, reloading curve, plastic strain and stress deterioration together determine the cyclic stress-strain model for FRP-confined concrete and will be further presented in the following sections.

It should be noted that Fig. 12 and the terminologies defined above are corresponding to the unloading occurring from the envelope curve. There are also the cases that the unloading may occur under the envelope curve, which is termed as the internal unloading-reloading cycle. Since it is not involved in the experimental investigation, this internal cyclic stress-strain model is also not discussed in the current study.

Envelope curve

It is widely accepted that the envelope curve of cyclically loaded FRP-confined concrete is close to the stress-strain curve of monotonically loaded FRP-confined concrete (Lam et al., 2006; Lam and Teng, 2009; Yu et al., 2015). Therefore, the envelope curve can be generated by the design-oriented model for monotonic compression. Most of the monotonic stress-strain models adopt a first parabolic stage and a second linear stage, with the smooth transition in between (Lam and Teng, 2009) as shown in Fig. 12. Lam and Teng's model (Lam and Teng, 2003) was adopted to generate the stress-strain ($\sigma_c - \varepsilon_c$) responses for FRP-confined HSC and ECC subjected to monotonic compression, with the following expressions:

$$\sigma_c = \begin{cases} E_c\varepsilon_c - \frac{(E_c - E_2)^2}{4f'_{c0}}\varepsilon_c^2 & (0 \le \varepsilon_c \le \varepsilon_t) \\ f'_{c0} + E_2\varepsilon_c & (\varepsilon_t < \varepsilon_c \le \varepsilon_{cu}) \end{cases} \tag{4}$$

in which E_c and f'_{c0} are compressive elastic modulus and strength of concrete without confinement. E_2 is the slope of the second linear portion and can be calculated as follows:

$$E_2 = \frac{f'_{cu} - f'_{c0}}{\varepsilon_{cu}} \tag{5}$$

where f'_{cu} and ε_{cu} are the ultimate compressive strength and the corresponding strain of FRP-confined concrete. ε_t is the transition strain between the first parabolic portion and the second linear portion, which can be calculated as follows:

$$\varepsilon_t = \frac{2f'_{c0}}{E_c - E_2} \tag{6}$$

Teng et al. (2009) developed the design equations of ultimate compressive strength f'_{cu} and ultimate axial strain ε_{cu} with the following formula forms:

$$\frac{f'_{cu}}{f'_{c0}} = C_1 + k_1(\rho_K - a)\rho_\varepsilon \tag{7}$$

$$\frac{\varepsilon_{cu}}{\varepsilon_{c0}} = C_2 + k_2 f(\rho_K) g(\rho_\varepsilon) \tag{8}$$

$$\rho_K = \frac{K_l}{f'_{c0}/\varepsilon_{c0}} = \frac{2E_f t_f}{\left(f'_{c0}/\varepsilon_{c0}\right)D} \tag{9}$$

$$\rho_\varepsilon = \frac{\varepsilon_{h,rup}}{\varepsilon_{c0}} \tag{10}$$

in which f'_{c0} and ε_{c0} are compressive strength and the corresponding strain of unconfined concrete; C_1 and C_2 are constants; k_1 and k_2 are strength and strain enhancement coefficients; ρ_K is confinement stiffness ratio between FRP and concrete; ρ_ε is termed as the strain ratio and reflects FRP strain capacity; a is defined as the threshold of effective confinement stiffness ratio; $f(\rho_K)$ and $g(\rho_\varepsilon)$ are expressions of ρ_K and ρ_ε. These formula forms have also been accepted by the UK Concrete Society (2021) and ACI 440.2R-17 (2017) as well as the literatures on FRP-confined concrete (Chen et al., 2021; Liao et al., 2022) with modifications on the coefficients to best-fit their test results. In this study, the same formula forms as shown in Eqs. (7-10) were used with the modifications on the coefficients based on the obtained test results to form the following equations for the predictions of ultimate compressive strength of HSC $f'_{cu,hsc}$ and ultimate compressive strength of ECC $f'_{cu,ecc}$:

$$\frac{f'_{cu,hsc}}{f'_{c0,hsc}} = 1 + 3.5(\rho_K - 0.035)\rho_\varepsilon \tag{11}$$

$$\frac{f'_{cu,ecc}}{f'_{c0,ecc}} = 1 + 2.5(\rho_K - 0.02)\rho_\varepsilon \tag{12}$$

where $f'_{c0,hsc}$ and $f'_{c0,ecc}$ are the compressive strengths of unconfined HSC and ECC, respectively. Strength enhancement coefficients k_1 in Eqs. (11) and (12) are taken to be 3.5 and 2.5, respectively, based on the recommendations of Teng et al. (2009) for FRP-confined normal concrete and Dang et al. (2020) for FRP-confined ECC. Confinement stiffness ratio thresholds a in Eqs. (11) and (12) are taken as 0.035 and 0.02, respectively, based on the regression of the obtained test data.

For ultimate axial strain of the composite column, the following expressions are proposed:

$$\frac{\varepsilon_{cu}}{\varepsilon_{c0,lrg}} = 1 + 1.71(\rho_{K,equ})^{0.56}(\rho_{\varepsilon,equ})^{1.85} \tag{13}$$

$$\rho_{K,equ} = \frac{K_l}{f'_{c0,ave}/\varepsilon_{c0,lrg}} = \frac{2E_f t_f}{\left(f'_{c0,ave}/\varepsilon_{c0,lrg}\right)D} \tag{14}$$

$$\rho_{\varepsilon,equ} = \frac{\varepsilon_{h,rup}}{\varepsilon_{c0,lrg}} \tag{15}$$

$$f'_{c0,ave} = \left(f'_{c0,hsc}A_{hsc} + f'_{c0,ecc}A_{ecc}\right) / (A_{hsc} + A_{ecc}) \tag{16}$$

$$\varepsilon_{c0,lrg} = \max(\varepsilon_{c0,hsc}, \varepsilon_{c0,ecc}) \tag{17}$$

in which $\rho_{K,equ}$ and $\rho_{\varepsilon,equ}$ are the equivalent confinement stiffness ratio and equivalent strain ratio, respectively. $\varepsilon_{c0,lrg}$ is the larger one between the compressive strains of unconfined HSC $\varepsilon_{c0,hsc}$ and ECC $\varepsilon_{c0,ecc}$. Since $\varepsilon_{c0,ecc}$ is larger than $\varepsilon_{c0,hsc}$ is this study, $\varepsilon_{c0,lrg}$ equals to $\varepsilon_{c0,ecc}$ for the FRP-ECC-HSC column. It considers the beneficial effect on the ultimate axial strain caused by the ECC ring. In Teng et al. (2009), $C_2 = 1.75$ is adopted for unconfined normal strength concrete with the strain at the peak stress of 0.002 and ultimate compressive strain of 0.0035. However, due to the brittleness of HSC that compressive stress will loss completely when reaching the peak stress and the typical compressive behavior of ECC that the compressive stress will drop significantly to yield a low residual stress when reaching the peak stress, $C_2 = 1$ is adopted in Eq. (13) to consider that the ultimate compressive strain is equal to the strain corresponding to the peak stress for unconfined HSC and ECC. The other parameters in Eq. (13), including the strain enhancement coefficient k_2 and the indices for $\rho_{K,equ}$ and $\rho_{\varepsilon,equ}$, are regressed based on the test results obtained from the current study.

With the design equations of ultimate compressive strength for HSC and ECC given in Eqs. (11) and (12), ultimate load capacity of FRP-confined HSC and FRP-ECC-HSC columns can be calculated with Eq. (3). Prediction results of the ultimate load capacity and ultimate axial strain for all the tested specimens are presented in Table 6 and Fig. 13. Close agreements through comparing the test results with predicted results can be obtained, with the mean value, coefficient of variation (CoV) value and coefficient of determination (R^2) value of 1.00, 0.056 and 0.73 for ultimate load capacity prediction and 1.00, 0.051 and 0.93 for ultimate axial strain prediction, respectively. All the predictions are within ±10% error, except that the specimen F10-E50-H90-25-C has a 12% higher ultimate load capacity prediction which is believed to be caused by the test data fluctuation. This demonstrates the good performance of the proposed equations on the prediction of the ultimate conditions. It should be noted that Eqs. (11-17) were recommended and validated using the test data obtained in the current study, in which the HSC core strength is in the range of 75.4 MPa to 96.8 MPa and the ECC ring strength is 55.2 MPa. The applicability of the equations may need to be further examined when a wider range of concrete strength is covered in future studies.

Eqs. (11-17) can be used in Eqs. (4-6) to generate the monotonic stress-strain curves for HSC core and ECC ring in the FRP-ECC-HSC composite column, followed by the determination of axial load-axial strain curves using Eq. (3). Predictions of the axial load-axial strain curve are generally in agreement with the corresponding test results as shown in Fig. 14. It also indicates that the presented monotonic stress-strain model (Eqs. (4-17)) can generate reasonable predictions on the envelope curve of FRP-ECC-HSC composite columns under cyclic compression.

Unloading curve

Unloading path for cyclically loaded FRP-confined concrete usually shows the approximately linear initial stage, followed by the nonlinear stage at the low stress level as shown in Fig. 12. Existing unloading models, which are able to capture the characteristics of the unloading curve, are summarized in Appendix I. In Lam and Teng's polynomial equation (Lam and Teng, 2009), the exponent η, which is related to the unloading strain ε_{un}, and the slope of unloading path at zero stress $E_{un,0}$, which is related to the unloading strain ε_{un} and concrete strength f'_{c0}, are the two parameters used to control the curve shape. Yu et al. (2015) adopted the same equation as Lam and Teng's model (Lam and Teng, 2009), but further considered concrete strength f'_{c0} in the calculation of the exponent η to better predict the unloading behavior of FRP-confined high strength concrete. Wang et al. (2012) and Hany et al. (2015) used the same equation for unloading prediction, with the curve shape featured by the exponent parameters B_0 and B_1. B_1 is related to unloading strain ε_{un} for both models. B_0 depends on the confining pressure in Wang et al.'s model (Wang et al., 2012). While in Hany et al.'s model (Hany et al., 2015), B_0 is assigned with a constant value. Li et al. (2018) developed the unloading equation considering the slope of unloading path at zero stress $E_{un,0}$ and the exponent m as the influencing parameters. $E_{un,0}$ and m are functions of concrete strength f'_{c0}, unloading strain ε_{un} and confinement rigidity ρ. All the unloading models are related to the plastic strain ε_{pl} as well.

These unloading models were used to calculate the unloading stress-strain curves for the HSC core and ECC ring respectively in the FRP-ECC-HSC composite column specimens. Axial load-axial strain curves can then be determined with Eq. (3) and evaluated through comparing with test results for the cyclically loaded specimens as shown in Fig. 15. As suggested by Zhang et al. (2015; 2021), it can be assumed that the load carried by the FRP tube reduces linearly to zero at the same time as the total load becomes zero in the unloading process. It is observed that unloading curves predicted by the above models are in good agreements with each other and can match well with the test curves, except for relatively larger deviations of Yu et al.'s model (Yu et al., 2015) at larger axial strains. It indicates that these existing unloading models can provide close predictions on the unloading curves for the FRP-confined HSC column and FRP-ECC-HSC composite column specimens.

It is noted that actual unloading strains and plastic strains were used in the calculation, so that the prediction accuracy only depends on the unloading model. Unloading stresses of HSC core and ECC ring cannot be determined directly in the FRP-ECC-HSC composite column. They were firstly calculated based on the corresponding envelope model as presented in the previous section with the unloading strain, followed by the determination of the unloading load with Eq. (3). The unloading load of the predicted curves was also kept the same as that of the test curve to ensure that it would not influence the comparison of the unloading model. Therefore, the same increment factor or reduction factor, which depends on the predicted value being lower or higher than the test value, was adopted for HSC and ECC to calculate the new unloading stresses that could ensure the unloading load of the predicted value being the same as that of the test value. The new unloading stresses of HSC and ECC were finally used for the unloading model calculation in Fig. 15.

Plastic strain

As a key parameter in the cyclic stress-stain model, plastic strain determines the location of the intersection point of unloading curve and zero-stress axis and has effect on the hysteresis curve shape. The existing prediction models of plastic strain for FRP-confined concrete are summarized in Appendix I. All the models considered a linear relation between plastic strain ε_{pl} and unloading strain ε_{un}, while Lam and Teng's model (Lam and Teng, 2009) and Li et al.'s model (Li et al., 2018) further took the effect of concrete strength f'_{c0} into consideration. Similar to the unloading model, Li et al. (2018) also related plastic strain ε_{pl} to the confinement rigidity ρ. Plastic strains of each unloading/reloading cycle for the tested specimens in this study are collected and plotted versus unloading strain in Fig. 16. It can be seen that the plastic strain increases with the increase of unloading strain, basically following the linear trend. Meanwhile, both the concrete strength and confinement rigidity have negligible effects on the plastic strain within the current test dataset. In order to better predict the relations between plastic strain and unloading strain, the following power function, which performs better than the linear function, is regressed based on the test data:

$$\varepsilon_{pl} = 1.386(\varepsilon_{un})^{1.16} - 0.00159 \tag{18}$$

Comparisons between test results and predictions generated by Eq. (18) and the existing models are presented in Fig. 17. Outstanding performance of the proposed equation can be observed with the mean value of 1.00 and CoV value of 0.089 for the ratio of test results to predicted results. On the contrary, the existing models could not provide satisfying predictions. Therefore, Eq. (18) will be used in this study to generate the plastic strain under each specific unloading strain.

Stress deterioration

As shown in Fig. 12, the stress σ_{new} at the reference point C in the reloading curve at the strain of ε_{ref}, which is the same as the unloading strain ε_{un}, is lower than the unloading stress σ_{un}. Stress deterioration φ, which is defined as follows, is used to reflect the damage behavior of concrete under cyclic loading:

$$\varphi = \frac{\sigma_{new}}{\sigma_{un}} \tag{19}$$

Appendix I summarizes that the φ is generally in the range of 0.912 to 0.938 for stress deterioration prediction. In this study, the stress deterioration is assumed to be the same for HSC core and ECC ring in the FRP-ECC-HSC composite column. The axial load carried by HSC core and ECC ring can be determined with Eq. (3), by subtracting the load carried by FRP tube from the total axial load. Therefore, stress deterioration for each loading cycle of the tested specimens can then be calculated based on the ratio of the axial load carried by the HSC and ECC ring at the strain ε_{ref} in the reloading curve to that at the strain ε_{un} in the unloading curve. In Fig. 18, it shows that the stress deterioration is generally irrelevant to concrete strength, confinement level and unloading strain. $\varphi = 0.923$ is regressed with the test data and will be used to generate the cyclic stress-strain models for HSC core and ECC ring under FRP confinement.

Reloading curve

The typical reloading path is characterized by a linear first portion and nonlinear second portion for FRP-confined concrete as shown in Fig. 12. The nonlinear portion could provide smooth transition from the linear portion to the envelope curve. In Appendix I, it summarizes equations for the existing reloading models. Wang et al. (2012) and Hany et al. (2015) adopted the linear equations from the reloading point to the envelope curve and omitted the nonlinear transition portion. The slope of the reloading curve is related to the unloading strain ε_{un}, plastic strain ε_{pl} and the new stress σ_{new} that is the product of the unloading stress σ_{un} and the stress deterioration φ. Lam and Teng (2009) and Yu et al. (2015) adopted the linear curve from the reloading point A to the reference point C, followed by a parabolic portion from the reference point C to point D where the reloading curve intersects with the envelope curve. In the parabolic portion, the slope at point C is the same as that of the first linear portion while the slope at point D is the same as that of the envelope curve. The equations are same for Lam and Teng's model (Lam and Teng, 2009) and Yu et al.'s model (Yu et al., 2015), only with different equations for plastic strain and stress deterioration. Li et al.'s reloading model (Li et al., 2018) adopted the four-parameter function, describing the nonlinear curve with two approximately linear portions and a nonlinear transition portion in between. Since Wang et al.'s model (Wang et al., 2012) and Hany et al.'s model (Wang et al., 2015) cannot describe the nonlinear parts of the reloading curve, they are not discussed in this study. Lam and Teng's and Yu et al.'s model (Lam and Teng, 2009; Yu et al., 2015) as well as Li et al.'s model (Li et al., 2018) will be evaluated with the newly proposed equations of plastic strain and stress deterioration in the following section.

Evaluation of proposed cyclic load-strain models

In previous sections, modified envelope model based on Lam and Teng's monotonic stress-strain model (Lam and Teng, 2003) was developed for HSC and ECC with the newly proposed equations for ultimate conditions. Five existing unloading models were evaluated and exhibited good performance on the predictions of the unloading curves of FRP-ECC-HSC composite columns, except that Yu et al.'s model (Yu et al., 2015) showed relatively larger deviations at larger axial strains. Equations of plastic strain and stress deterioration were proposed based on the test data obtained in this study. Five existing reloading models were introduced and Lam and Teng's and Yu et al.'s model (Lam and Teng, 2009; Yu et al., 2015) as well as Li et al.'s model (Li et al., 2018) were selected for capturing the features of the reloading curve in a more accurate manner. With these components determined, cyclic stress-strain models can be obtained for FRP-confined HSC and ECC. Furthermore, cyclic axial load-axial strain curves can be calculated with Eq. (3). In the calculation, the load carried by FRP tube is determined by the stress-strain relation obtained from FRP ring compression tests in the reloading process and is considered to decrease linearly in the unloading process.

Predicted curves are plotted and compared with test curves in Fig. 19. Because of the similar performance of the five presented unloading models, only Lam and Teng's model (Lam and Teng, 2009) and Li et al.'s model (Li et al., 2018) were adopted to match with the corresponding reloading models by Lam and Teng (2009) and Li et al. (2018). In Fig. 19, Model I represents the cyclic model consisting of the modified envelope curve model, Lam and Teng's unloading and reloading models (Lam and Teng, 2009), as well as the proposed equations of plastic strain and stress deterioration; Model II represents the cyclic model consisting of the modified envelope model, Li et al.'s unloading and reloading models (Li et al., 2018), as well as the proposed equations of plastic strain and stress deterioration. It should be noted that all the other parameters used are calculated by the cyclic models, except for the actual unloading strain for each loading cycle. It can be observed that the cyclic load-strain curves predicted by Model I could agree well with the test curves, in terms of the envelope curves, plastic strains, unloading curves and reloading curves. For Model II, however, the predicted reloading curves present larger deviations compared with test curves. It indicates that Li et al.'s model (Li et al., 2018) cannot provide close reloading predictions within the scope of the current test data. Although Li et al.'s model (Li et al., 2018) could describe the features of the reloading curves, the predicted reloading slopes are not in line with the test results. Meanwhile, the reloading curve calculated by Li et al.'s model (Li et al., 2018) cannot intersect with the envelope curve for most of the tested specimens. The reloading process will end, and the next unloading process will start when the next unloading strain is reached. For Model II, the unloading stresses (except for the first one) are calculated based on the reloading model, instead of the envelope model, with the corresponding unloading strains. Therefore, the proposed Model I can be adopted to predict the load-strain behavior of the FRP-ECC-HSC composite columns under cyclic compression.

Conclusions

Cyclic compressive behavior of the innovative FRP-ECC-HSC composite column was experimentally investigated in this study. Test variables including HSC core strength, FRP tube thickness and ECC ring thickness were examined. Typical failure modes, dilation behavior and axial load versus axial strain responses were discussed. Cyclic load-strain models were developed to predict the compressive behavior of the composite columns. Based on the reported test data, the following conclusions can be drawn within the current scope of this study:

(1) ECC ring could realize a more uniform hoop strain distribution in the FRP-ECC-HSC composite columns. The average FRP rupture strain was improved, and column failure was consequently delayed. Compared with the corresponding FRP-confined HSC columns, FRP-ECC-HSC composite columns exhibited 0.7-69.1% larger ultimate axial strains, indicating the enhanced column deformability.

(2) It was observed from the test results that the ultimate axial strain would increase with the increase of ECC thickness while decrease with the increase of HSC core strength. Both ultimate compressive strength and ultimate axial strain increased with the increase of FRP tube thickness. For cyclically loaded columns, the investigated test variables could influence the unloading and reloading curves and were considered in the corresponding prediction models. However, plastic strain and stress deterioration were found to be independent of the test variables.

(3) Hoop strain distribution for cyclically loaded columns was generally more uniform in comparison to the corresponding monotonically loaded columns. Both FRP-confined HSC columns and FRP-ECC-HSC composite columns under cyclic compression could develop the larger ultimate axial strain than those under monotonic compression.

(4) With the proposed equation of axial load, load-strain curves of the FRP-ECC-HSC composite columns can be generated based on the stress-strain curves of FRP-confined HSC and ECC. Lam and Teng's monotonic stress-strain model was modified with the proposed equations of ultimate conditions. It can provide close predictions on the load-strain behavior for the monotonically loaded columns and can be used to predict the envelope curves for the cyclically loaded columns.

(5) Existing unloading and reloading models were evaluated and selected to predict the unloading and reloading curves for the tested columns. New equations of plastic strain and stress deterioration were proposed based on the test results obtained in this study. Two proposed cyclic load-strain models were used to generate the axial load-axial curves for the cyclically loaded columns. It shows that Model I could provide close predictions compared with test results.

Appendix I: Existing cyclic stress-strain models for FRP-confined concrete

Objects	Lam and Teng (2009)	Yu et al. (2015)	Wang et al. (2012)	Hany et al. (2015)	Li et al. (2018)
Unloading model	$\sigma_c = a\varepsilon_c^{\eta} + b\varepsilon_c + c$ $a = \frac{\sigma_{un}-E_{un,0}(\varepsilon_{un}-\varepsilon_{pl})}{\varepsilon_{un}^{\eta}-\varepsilon_{pl}^{\eta}-\eta\varepsilon_{pl}^{\eta-1}(\varepsilon_{un}-\varepsilon_{pl})}$ $b = E_{un,0} - \eta\varepsilon_{pl}^{\eta-1}a$ $c = -a\varepsilon_{pl}^{\eta} - b\varepsilon_{pl}$ $E_{un,0} = \min(\frac{0.5f'_{c0}}{\varepsilon_{un}}, \frac{\sigma_{un}}{\varepsilon_{un}-\varepsilon_{pl}})$ $\eta = 350\varepsilon_{un} + 3$	Same as Lam and Teng (2009) except for η $\eta = 40(350\varepsilon_{un} + 3)/f'_{c0}$	$\frac{\sigma_c}{\sigma_{un}} = B_0(\frac{\varepsilon_c-\varepsilon_{pl}}{\varepsilon_{un}-\varepsilon_{pl}})^{B_1} + (1-B_0)(\frac{\varepsilon_c-\varepsilon_{pl}}{\varepsilon_{un}-\varepsilon_{pl}})$ $B_0 = 0.5 + 0.3(\frac{f_l}{f'_{c0}})^{0.07} - 0.1(\frac{f_{ls}}{f'_{c0}})^{0.04}$ for $\varepsilon_{un} \leq 0.02$, $B_1 = -0.02\left(\frac{\varepsilon_{un}}{\varepsilon_{c0}}\right)^2 + 0.46\left(\frac{\varepsilon_{un}}{\varepsilon_{c0}}\right) + 1.76$ for $\varepsilon_{un} > 0.02$, $B_1 = 4.36$	$\frac{\sigma_c}{\sigma_{un}} = B_0(\frac{\varepsilon_c-\varepsilon_{pl}}{\varepsilon_{un}-\varepsilon_{pl}})^{B_1} + (1-B_0)(\frac{\varepsilon_c-\varepsilon_{pl}}{\varepsilon_{un}-\varepsilon_{pl}})$ $B_0 = 0.8$ $B_1 = 2.172\left(\frac{\varepsilon_{un}}{\varepsilon_{c0}}\right)^{0.324}$	$\sigma_c = E_{un,0}\left(\frac{\varepsilon_c}{\varepsilon_{pl}}\right)^m(\varepsilon_c - \varepsilon_{pl})$ $\frac{E_{un,0}}{E_c} = 0.21(\frac{f'_{c0}}{f'_{30}})^{0.195}\rho^{-0.031}(\frac{\varepsilon_{un}}{\varepsilon_{c0}})^{-1.115}$ $m = \log_{(\frac{\varepsilon_{un}}{\varepsilon_{pl}})}(\frac{\sigma_{un}}{E_{un,0}(\varepsilon_{un}-\varepsilon_{pl})})$
Plastic strain	for $0 < \varepsilon_{un} \leq 0.001$, $\varepsilon_{pl} = 0$ for$0.001 < \varepsilon_{un} < 0.0035$, $\varepsilon_{pl} = [1.4(0.87 - 0.004f'_{c0}) - 0.64](\varepsilon_{un} - 0.001)$ for $0.0035 \leq \varepsilon_{un} \leq \varepsilon_{cu}$, $\varepsilon_{pl} = (0.87 - 0.004f'_{c0})\varepsilon_{un} - 0.0016$	for $0 < \varepsilon_{un} \leq 0.001$, $\varepsilon_{pl} = 0$ for $0.001 < \varepsilon_{un} \leq 0.0035$, $\varepsilon_{pl} = 0.184\varepsilon_{un} - 0.0002$ for $0.0035 < \varepsilon_{un} \leq \varepsilon_{cu}$, $\varepsilon_{pl} = 0.703\varepsilon_{un} - 0.002$	for $0 < \varepsilon_{un} \leq 0.001$, $\varepsilon_{pl} = 0$ for $0.001 < \varepsilon_{un} \leq 0.004$, $\varepsilon_{pl} = 0.42\varepsilon_{un} - 0.0004$ for $0.004 < \varepsilon_{un} \leq \varepsilon_{cu}$, $\varepsilon_{pl} = 0.815\varepsilon_{un} - 0.002$	for $0 < \varepsilon_{un} \leq 0.001$, $\varepsilon_{pl} = 0$ for $0.001 < \varepsilon_{un} \leq 0.0035$, $\varepsilon_{pl} = 0.4552\varepsilon_{un} - 0.0003$ for $0.0035 < \varepsilon_{un} \leq \varepsilon_{cu}$, $\varepsilon_{pl} = 0.7827\varepsilon_{un} - 0.0014$	for $0 < \varepsilon_{un} \leq 0.001$, $\varepsilon_{pl} = 0$ for $0.001 < \varepsilon_{un} \leq \varepsilon_{cu}$, $\varepsilon_{pl} = 0.353\left(\frac{f'_{c0}}{f'_{30}}\right)^{-0.4}(\varepsilon_{un} - 0.001) +$ $3.36\rho^{-0.178}(\varepsilon_{un} - 0.001)^{1.414}$
Stress deterioration	for $0 < \varepsilon_{un} \leq 0.001$, $\varphi = 1$ for $0.001 < \varepsilon_{un} < 0.002$, $\varphi = 1 - 80(\varepsilon_{un} - 0.001)$ for $0.002 \leq \varepsilon_{un} \leq \varepsilon_{cu}$, $\varphi = 0.92$	for $0 < \varepsilon_{un} \leq 0.001$, $\varphi = 1$ for $0.001 < \varepsilon_{un} \leq 0.0035$, $\varphi = 1 - 32(\varepsilon_{un} - 0.001)$ for $0.0035 < \varepsilon_{un} \leq \varepsilon_{cu}$, $\varphi = 0.92$	$\varphi = 0.912$	for $0 < \varepsilon_{un} \leq 0.001$, $\varphi = 1$ for $0.001 < \varepsilon_{un} \leq \varepsilon_{cu}$, $\varphi = 0.938$	N.A.
Reloading model	for $\varepsilon_{re} \leq \varepsilon_c \leq \varepsilon_{ref}$, $\sigma_c = \sigma_{re} + E_{re}(\varepsilon_c - \varepsilon_{re})$ for $\varepsilon_{ref} \leq \varepsilon_c \leq \varepsilon_{ret,env}$, $\sigma_c = A{\varepsilon_c}^2 + B\varepsilon_c + C$ $E_{re} = (\sigma_{new} - \sigma_{re})/(\varepsilon_{ref} - \varepsilon_{re})$ $\sigma_{new} = \varphi\sigma_{un}$ $B = E_{re} - 2A\varepsilon_{ref}$ $C = \sigma_{new} - A{\varepsilon_{ref}}^2 - B\varepsilon_{ref}$ for $\varepsilon_{ret,env} < \varepsilon_t$, $A = \frac{(E_C-E_2)^2(E_{re}\varepsilon_{ref}-\sigma_{new})+(E_C-E_{re})^2f'_{c0}}{4(\sigma_{new}-E_C\varepsilon_{ref})f'_{c0}+(E_C-E_2)^2{\varepsilon_{ref}}^2}$ $\varepsilon_{ret,env} = \frac{E_C-B}{2A+\frac{(E_C-E_2)^2}{f'_{c0}}}$ for $\varepsilon_{ret,env} \geq \varepsilon_t$, $A = \frac{(E_{re}-E_2)^2}{4(\sigma_{new}-f'_{c0}-E_2\varepsilon_{ref})}$ $\varepsilon_{ret,env} = \frac{E_2-B}{2A}$	Same as Lam and Teng (2009)	$\sigma_c = E_{re}(\varepsilon_c - \varepsilon_{pl})$ $E_{re} = \frac{\sigma_{new}}{\varepsilon_{un}-\varepsilon_{pl}}$ $\sigma_{new} = \varphi\sigma_{un}$	$\sigma_c = E_{re}(\varepsilon_c - \varepsilon_{pl})$ $E_{re} = \frac{\sigma_{new}}{\varepsilon_{un}-\varepsilon_{pl}}$ $\sigma_{new} = \varphi\sigma_{un}$	$\sigma_c = \frac{(E_{re}-E_2)(\varepsilon_c-\varepsilon_{pl})}{(1+(\frac{(E_{re}-E_2)(\varepsilon_c-\varepsilon_{pl})}{f_r})^n)^{1/n}} + E_2(\varepsilon_c - \varepsilon_{pl})$ $\frac{E_{re}}{E_c} = (\frac{f'_{c0}}{f'_{30}})^{0.032}\bar{\varepsilon}^{-0.409} - 0.317\rho^{-0.064\bar{\varepsilon}}$ for $E_2 \geq 0$, $\frac{f_r}{f'_{c0}} = 0.693\frac{\sigma_{un}}{f'_{c0}} + 0.337\rho^{-0.053}$ for $E_2 < 0$, $\frac{f_r}{f'_{c0}} = 0.969\frac{\sigma_{un}}{f'_{c0}} + 1.981\rho^{-2.012}$ $\bar{\varepsilon} = \varepsilon_{un}/\varepsilon_{c0} \leq 10$ $n = 2.61\left(\frac{\varepsilon_{un}}{\varepsilon_{c0}}\right) + 4.88$

Data Availability Statement

Some or all data, models, or codes that support the findings of this study are available from the corresponding author upon reasonable request.

Acknowledgements

The research work presented in this paper was supported by the Research Grants Council of the Hong Kong Special Administrative Region, China – Theme-based Research Scheme (Project No. T22-502/18-R).

References

Abdallah, A. E., and E. F. El-Salakawy. 2022. "Seismic performance of GFRP-RC circular columns with different aspect ratios and concrete strengths." *Eng. Struct.* 257: 114092. https://doi.org/10.1016/j.engstruct.2022.114092.

American Concrete Institute ACI. 2017. "Guide for the design and construction of externally bonded FRP systems for strengthening concrete structures." ACI-440 2R, Farmington Hills, Mich.

ASTM C192. 2019. "Standard practice for making and curing concrete test specimens in the laboratory." American Society for Testing and Materials, Philadelphia, USA.

ASTM C31. 2019. "Standard practice for making and curing concrete test specimens in the field." American Society for Testing and Materials, Philadelphia, USA.

ASTM D2290. 2008. "Standard test method for apparent hoop tensile strength of plastic or reinforced plastic pipe by split disk method." American Society for Testing and Materials, Philadelphia, USA.

Bai, Y. L., J. G. Dai, and T. Ozbakkaloglu. 2017. "Cyclic stress-strain model incorporating buckling effect for steel reinforcing bars embedded in FRP-confined concrete." *Compos. Struct.* 182: 54-66. https://doi.org/10.1016/j.compstruct.2017.09.007.

Bai, Y. L., S. J. Mei, P. Li, and J. Xu. 2021. "Cyclic stress-strain model for large-rupture strain fiber-reinforced polymer(LRS FRP)-confined concrete." *J. Build. Eng.* 42: 102459. https://doi.org/10.1016/j.jobe.2021.102459.

Chen, G., Y. Wang, T. Yu, B. Wan, B. Zhang, and Q. Liu. 2021. "Behavior and design-oriented model for elliptical FRP-confined concrete under axial compression." *Eng. Struct.* 249: 113387. https://doi.org/10.1016/j.engstruct.2021.113387.

Concrete Society. 2012. "Design guidance for strengthening concrete structures with fibre composite materials." Technical Rep. No. 55, 3rd Ed., Crowthorne, Berkshire, U.K.

Dang, Z., P. Feng, J. Q. Yang, and Q. Zhang. 2020. "Axial compressive behavior of engineered cementitious composite confined by fiber-reinforced polymer." *Compos. Struct.* 243: 112191. https://doi.org/10.1016/j.compstruct.2020.112191.

GB/T5350. 2005. "Fiber-Reinforced Thermosetting Plastic Composites Pipe: Determination for Longitudinal Compressive Properties." The Standards Press of China.

Hany, N. F., E. G. Hantouche, and M. H. Harajli. 2015. "Axial stress-strain model of CFRP-confined concrete under monotonic and cyclic loading." *J. Compos. Constr.* 19 (6): 04015004. https://doi.org/10.1061/(ASCE)CC.1943-5614.0000557.

Japan Society of Civil Engineers (JSCE). 2008. "Recommendations for design and construction of high performance fiber reinforced cement composites with multiple fine cracks (HPFRCC)." Concrete Engineering Series 82, 2008.

Lai, M. H., Y. W. Liang, Q. Wang, F. M. Ren, M. T. Chen, and J. C. M. Ho. 2020. "A stress-path dependent stress-strain model for FRP-confined concrete." *Eng. Struct.* 203: 109824. https://doi.org/10.1016/j.engstruct.2019.109824.

Lam, L., and J. G. Teng. 2003. "Design-oriented stress-strain model for FRP-confined concrete." *Constr. Build. Mater.* 17 (6): 471-489. https://doi.org/10.1016/S0950-0618(03)00045-X.

Lam, L., and J. G. Teng. 2009. "Stress–strain model for FRP-confined concrete under cyclic axial compression." *Eng. Struct.* 31: 308–321. https://doi.org/10.1016/j.engstruct.2008.08.014.

Lam, L., J. G. Teng, J. G. Cheung, and Y. Xiao. 2006. "FRP-confined concrete under axial cyclic compression." *Cem. Concr. Compos.* 28 (10): 949–958. https://doi.org/10.1016/j.cemconcomp.2006.07.007.

Lee, C. K., M. K. I. Khan, Y. X. Zhang, and M. M. Rana. 2020. "Compressive performance of ECC-concrete encased high strength steel composite columns." *Eng. Struct.* 213: 110567. https://doi.org/10.1016/j.engstruct.2020.110567.

Li, L. Z., Y. Bai, K. Q. Yu, J. T. Yu, and Z. D. Lu. 2019. "Reinforced high-strength engineered cementitious composite (ECC) columns under eccentric compression: Experiment and theoretical model." *Eng. Struct.* 198: 109541. https://doi.org/10.1016/j.engstruct.2019.109541.

Li, P., Y. F. Wu, Y. Zhou, and F. Xing. 2018. "Cyclic stress-strain model for FRP-confined concrete considering post-peak softening." *Compos. Struct.* 201: 902-915. https://doi.org/10.1016/j.compstruct.2018.06.088.

Li, S., T. M. Chan, and B. Young. 2022a. "Behavior of GFRP-concrete double tube composite columns." *Thin-Walled Struct.* 178: 109490. https://doi.org/10.1016/j.tws.2022.109490.

Li, S., T. M. Chan, and B. Young. 2022b. "Compressive behavior and analysis-oriented model of FRP-confined engineered cementitious composite columns." *Eng. Struct.* 270: 114869. https://doi.org/10.1016/j.engstruct.2022.114869.

Li, S., T. M. Chan, and B. Young. 2023. “Experimental investigation on axial compressive behavior of novel FRP-ECC-HSC composite short column.” Compos. Struct. 303: 116285. https://doi.org/10.1016/j.compstruct.2022.116285.

Li, V. C., S. Wang, and C. Wu. 2001. “Tensile strain-hardening behavior of polyvinyl alcohol engineered cementitious composite (PVA-ECC).” *ACI Mater. J.* 98 (6): 483–92.

Li, Y. L., and Zhao X. L. 2020. “Hybrid double tube sections utilising seawater and sea sand concrete, FRP and stainless steel.” *Thin-Walled Struct.* 149: 106643. https://doi.org/10.1016/j.tws.2020.106643.

Liao, J., J. J. Zeng, Q. M. Gong, W. M. Quach, W. Y. Gao, and L. Zhang. 2022. “Design-oriented stress-strain model for FRP-confined ultra-high performance concrete (UHPC).” *Constr. Build. Mater.* 2022 318: 126200. https://doi.org/10.1016/j.conbuildmat.2021.126200.

Nguyen, C. L., and C. K. Lee. 2021. “Flexural behaviours of Engineered Cementitious Composites – High strength steel composite beams.” *Eng. Struct.* 249: 113324. https://doi.org/10.1016/j.engstruct.2021.113324.

Ozbakkaloglu, T., J. C. Lim and T. Vincent. 2013. “FRP-confined concrete in circular sections: Review and assessment of stress–strain models.” *Eng. Struct.* 49: 1068–1088. https://doi.org/10.1016/j.engstruct.2012.06.010.

Pessiki, S., K. A. Harries, J. T. Kestner, R. Sause, and J. M. Ricles. 2001. “Axial behavior of reinforced concrete columns confined with FRP jackets.” *J. Compos. Constr.* 5 (4): 237-245. https://doi.org/10.1061/(ASCE)1090-0268(2001)5:4(237).

Pour, A. F., T. Ozbakkaloglu, T. Vincent. 2018. “Simplified design-oriented axial stress-strain model for FRP-confined normal- and high-strength concrete.” *Eng. Struct.* 175: 501-516. https://doi.org/10.1016/j.engstruct.2018.07.099.

Shao, Y., Z. Zhu, and A. Mirmiran. 2006. “Cyclic modeling of FRP-confined concrete with improved ductility.” *Cem. Concr. Compos.* 28 (10): 959–968. https://doi.org/10.1016/j.cemconcomp.2006.07.009.

Sirach, N., S. T. Smith, T. Yu, and A. Mostafa. 2021. “Experimental study on the confinement of concrete cylinders with large rupture-strain FRP composites.” *J. Compos. Constr.* 25 (4): 04021026. https://doi.org/10.1061/(ASCE)CC.1943-5614.0001137.

Teng, J. G., T. Jiang, L. Lam, and Y. Z. Luo. 2009. “Refinement of a design-oriented stress–strain model for FRP-confined concrete.” *J. Compos. Constr.* 13 (4): 269-278. https://doi.org/10.1061/(ASCE)CC.1943-5614.0000012.

Wang, Z., D. Wang, S. T. Smith, and D. Lu. 2012. “Experimental testing and analytical modeling of CFRP-confined large circular RC columns subjected to cyclic axial compression.” *Eng. Struct.* 40: 64-74. https://doi.org/10.1016/j.engstruct.2012.01.004.

Wu, Y. F., and J. F. Jiang. 2013. "Effective strain of FRP for confined circular concrete columns." *Compos. Struct.* 95: 479-491. https://doi.org/10.1016/j.compstruct.2012.08.021.

Xie, J., Z. Wang, and J. B. Yan. 2022. "Axial compression behaviours of seawater and sea sand concrete-filled GFRP stub tubes at arctic low temperatures." *Thin-Walled Struct*. 170: 108566. https://doi.org/10.1016/j.tws.2021.108566.

Xu, L. Y., B. T. Huang, V. C. Li, and J. G. Dai. 2022. "High-strength high-ductility Engineered/Strain-Hardening Cementitious Composites (ECC/SHCC) incorporating geopolymer fine aggregates." *Cem. Concr. Compos.* 125: 104296. https://doi.org/10.1016/j.cemconcomp.2021.104296.

Yang, J. Q., and P. Feng. 2021. "Analysis-oriented model for FRP confined high-strength concrete: 3D interpretation of path dependency." *Compos. Struct.* 278: 114695. https://doi.org/10.1016/j.compstruct.2021.114695.

Yu, T., B. Zhang, and J. G. Teng. 2015. "Unified cyclic stress–strain model for normal and high strength concrete confined with FRP." *Eng. Struct.* 102: 189-201. https://doi.org/10.1016/j.engstruct.2015.08.014.

Yuan, W. Y., Q. Han, Y. L. Bai, X. L. Du, and Z. W. Yan. 2021. "Compressive behavior and modelling of engineered cementitious composite (ECC) confined with LRS FRP and conventional FRP." *Compos. Struct.* 272: 114200. https://doi.org/10.1016/j.compstruct.2021.114200.

Zeng, J. J., J. Liao, Y. Y. Ye, Y. C. Guo, Y. Zhang, and L. H. Tan. 2021. "Behavior of FRP spiral strip-confined concrete under cyclic axial compression." *Constr. Build. Mater.* 295: 123544. https://doi.org/10.1016/j.conbuildmat.2021.123544.

Zhang, B., J. G. Teng, and T. Yu. 2017. "Compressive behavior of double-skin tubular columns with high-strength concrete and a filament-wound FRP tube." *J. Compos. Constr*. 21 (5): 04017029. https://doi.org/10.1061/(ASCE)CC.1943-5614.0000800.

Zhang, B., T. Yu, and J. G. Teng. 2015. "Behavior of concrete-filled FRP tubes under cyclic axial compression." *J. Compos. Constr*. 19 (3): 04014060. https://doi.org/10.1061/(ASCE)CC.1943-5614.0000523.

Zhang, B., T. Yu, and J. G. Teng. 2021. "Behavior and modelling of FRP-concrete-steel hybrid double-skin tubular columns under repeated unloading/reloading cycles." *Compos. Struct.* 258: 113393. https://doi.org/10.1016/j.compstruct.2020.113393.

Zhang, Y., Y. Wei, K. Miao, and B. Li. 2022. "A novel seawater and sea sand concrete-filled FRP-carbon steel composite tube column: Cyclic axial compression behaviour and modelling." *Eng. Struct.* 252: 113531. https://doi.org/10.1016/j.engstruct.2021.113531.

Zhou, J. K., G. Lin, and J. G. Teng. 2021. "Compound concrete-filled FRP tubular columns under cyclic axial compression." *Compos. Struct.* 275: 114329. https://doi.org/10.1016/j.compstruct.2021.114329.

Zhu, J. Y., G. Lin, J. G. Teng, T. M. Chan, J. J. Zeng, and L. J. Li. 2020. “FRP-Confined square concrete columns with section curvilinearization under axial compression.” *J. Compos. Constr.* 24 (2): 04020004. https://doi.org/10.1061/(ASCE)CC.1943-5614.0000999.

Table 1. Concrete mix proportions (kg/m^3)

Concrete	Water	Cement	Fly ash	Sand	Agg-10	Agg-20	S.P.*	Fiber
C70	133	550	-	693	410	613	8.8	-
C90	120	603	-	693	410	613	10.6	-
ECC50	310.5	554.4	665.2	443.7	-	-	13.5	19.4

S.P.*: Super plasticizer.

Table 2. Concrete material properties

Concrete	Compressive cylinder strength (MPa)	Compressive strain	Elastic modulus (GPa)	Poisson's ratio
C70	75.4	0.0028	32.0	0.21
C90	96.8	0.0032	35.3	0.21
ECC50	55.2	0.0046	15.3	0.21

Table 3. Polyethylene (PE) fiber properties

Diameter (μm)	Length (mm)	Density (g/cm^3)	Elastic modulus (GPa)	Tensile strength (MPa)
24	12	0.97	120	3000

Table 4. FRP tube material properties

FRP tube	Thickness (mm)	Hoop tensile properties			Axial compressive properties		
		Strength (MPa)	Strain	Elastic modulus (GPa)	Strength (MPa)	Strain	Elastic modulus (GPa)
F7	2.5	620.8	0.0156	39.8	70.6	0.0106	9.5
F10	3.5	630.9	0.0164	38.5	84.6	0.0111	9.7

Table 5. Key results of tested specimens

Specimen label	F_1 (kN)	F_c (kN)	ε_{cu}	$\varepsilon_{h,rup}$	f_{lu} (MPa)	F_c/F_1	$\varepsilon_{cu}/\varepsilon_{c0}$
F7-H70-M*	2777	2792	0.0144	0.0116	11.5	1.01	5.14
F7-H70-C	2664	2817	0.0152	0.0125	12.4	1.06	5.43
F7-E50-H70-15-M*	2506	2773	0.0145	0.0117	11.6	1.11	5.18
F7-E50-H70-15-C	2653	2731	0.0182	0.0146	14.5	1.03	6.50
F7-E50-H70-25-M*	2194	2707	0.0209	0.0143	14.2	1.23	7.46
F7-E50-H70-25-C	-	2718	0.0257	0.0180	17.9	-	9.18
F7-H90-M*	3195	3166	0.0123	0.0117	11.6	0.99	3.84
F7-H90-C1	3056	3134	0.0136	0.0126	12.5	1.03	4.25
F7-H90-C2	3279	3084	0.0149	0.0134	13.3	0.94	4.66
F7-E50-H90-15-M*	2980	3021	0.0137	0.0125	12.4	1.01	4.28
F7-E50-H90-15-C1	2935	2899	0.0138	0.0132	13.1	0.99	4.31
F7-E50-H90-15-C2	2904	2726	0.0155	0.0130	12.9	0.94	4.84
F7-E50-H90-25-M*	2579	2809	0.0152	0.0133	13.2	1.09	4.75
F7-E50-H90-25-C1	2690	2733	0.0167	0.0143	14.2	1.02	5.22
F7-E50-H90-25-C2	2654	2674	0.0142	0.0122	12.1	1.01	4.44
F10-H90-M*	3446	3730	0.0130	0.0117	15.8	1.08	4.06
F10-H90-C1	3358	3563	0.0133	0.0114	15.4	1.06	4.16
F10-H90-C2	3494	3626	0.0149	0.0127	17.1	1.04	4.66
F10-E50-H90-15-M*	2985	3361	0.0167	0.0124	16.7	1.13	5.22
F10-E50-H90-15-C	3127	3303	0.0181	0.0129	17.4	1.06	5.66
F10-E50-H90-25-M*	2766	3196	0.0187	0.0130	17.5	1.16	5.84
F10-E50-H90-25-C	2955	3065	0.0216	0.0148	19.9	1.04	6.75

*Note: The test data for monotonic loading were firstly reported by the authors in Li et al. (2023).

Table 6. Predictions on ultimate conditions for tested specimens

Specimen label	Ultimate load capacity (kN)			Ultimate axial strain		
	$F_{c,test}$	$F_{c,pred}$	$F_{c,test}/F_{c,pred}$	$\varepsilon_{cu,test}$	$\varepsilon_{cu,pred}$	$\varepsilon_{cu,test}/\varepsilon_{cu,pred}$
F7-H70-M	2792	2547	1.10	0.0144	0.0133	1.09
F7-H70-C	2817	2552	1.10	0.0152	0.0148	1.03
F7-E50-H70-15-M	2773	2545	1.09	0.0145	0.0142	1.02
F7-E50-H70-15-C	2731	2605	1.05	0.0182	0.0191	0.95
F7-E50-H70-25-M	2707	2619	1.03	0.0209	0.0189	1.10
F7-E50-H70-25-C	2718	2727	1.00	0.0257	0.0265	0.97
F7-H90-M	3166	3070	1.03	0.0123	0.0121	1.02
F7-H90-C1	3134	3063	1.02	0.0136	0.0134	1.01
F7-H90-C2	3084	3058	1.01	0.0149	0.0146	1.02
F7-E50-H90-15-M	3021	2931	1.03	0.0137	0.0143	0.96
F7-E50-H90-15-C1	2899	2939	0.99	0.0138	0.0154	0.90
F7-E50-H90-15-C2	2726	2937	0.93	0.0155	0.0151	1.03
F7-E50-H90-25-M	2809	2873	0.98	0.0152	0.0160	0.95
F7-E50-H90-25-C1	2733	2895	0.94	0.0167	0.0176	0.95
F7-E50-H90-25-C2	2674	2848	0.94	0.0142	0.0143	0.99
F10-H90-M	3730	3600	1.04	0.0130	0.0137	0.95
F10-H90-C1	3563	3590	0.99	0.0133	0.0133	1.00
F10-H90-C2	3626	3632	1.00	0.0149	0.0155	0.96
F10-E50-H90-15-M	3361	3450	0.97	0.0167	0.0159	1.05
F10-E50-H90-15-C	3303	3473	0.95	0.0181	0.0168	1.08
F10-E50-H90-25-M	3196	3384	0.94	0.0187	0.0176	1.06
F10-E50-H90-25-C	3065	3484	0.88	0.0216	0.0211	1.02
Mean			1.00			1.00
CoV			0.056			0.051
R^2			0.73			0.93

List of Figure Captions

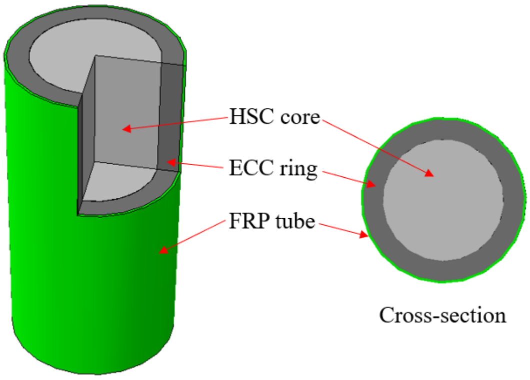

Fig. 1. FRP-ECC-HSC composite column.

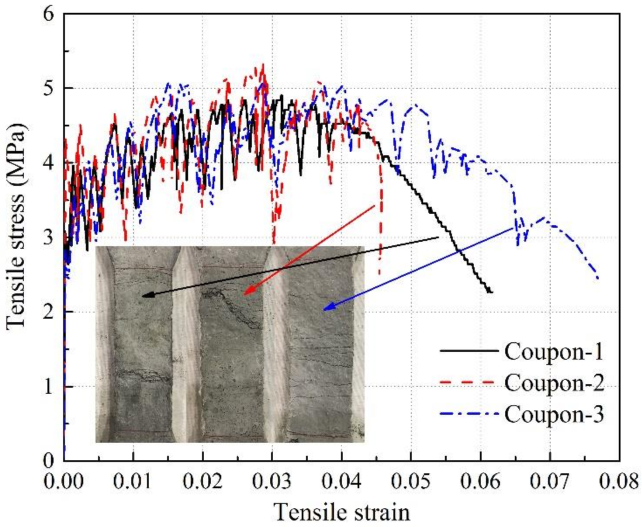

Fig. 2. Tensile behavior of ECC coupons.

Fig. 3. Preparation process of FRP-ECC-HSC composite columns in laboratory: (a) HSC core casting; (b) Placing HSC core inside FRP tube; (c) After pouring ECC; (d) Capping of two ends.

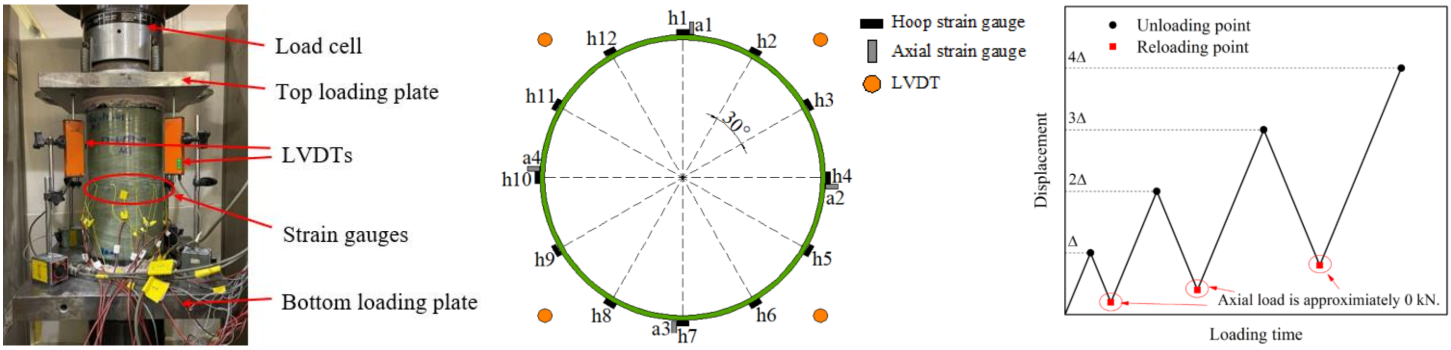

(a) Test setup (b) Specimen instrumenttion (c) Cyclic loading scheme

Fig. 4. Test setup, specimen instrumentation and loading scheme.

F7-H70-M F10-H90-C1 F7-E50-H70-25-M F7-E50-H70-15-C F7-E50-H70-25-C F10-E50-H90-15-C F10-E50-H90-25-C

(a) FRP rupture

F7-H70-M F10-H90-C1 F7-E50-H70-25-M F7-E50-H70-15-C F7-E50-H70-25-C F10-E50-H90-15-C F10-E50-H90-25-C

(b) Cracking behavior of inner concrete (with FRP tubes removed)

Fig. 5. Typical failure modes of tested specimens.

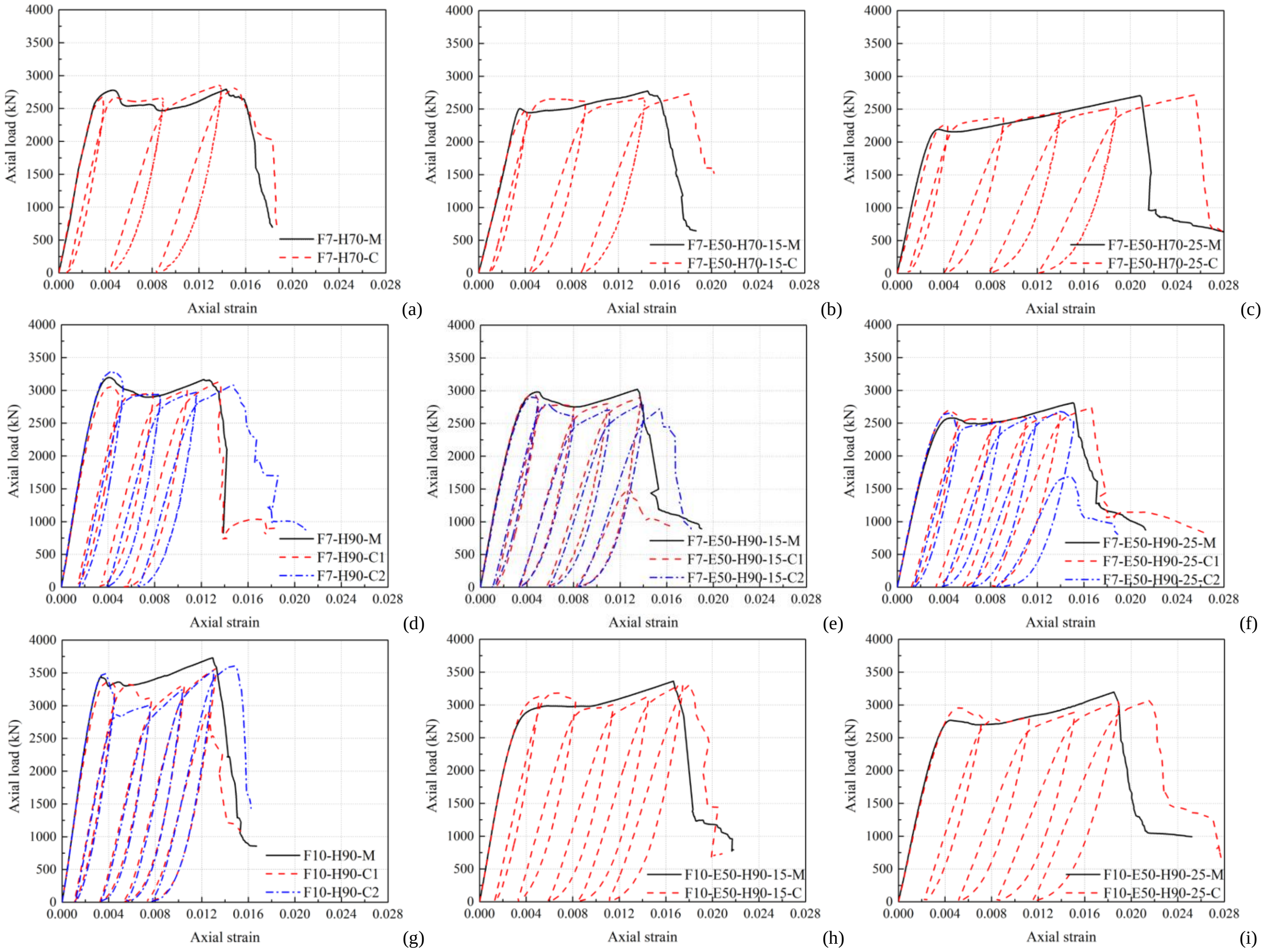

Fig. 6. Axial load-axial strain curves for tested specimens.

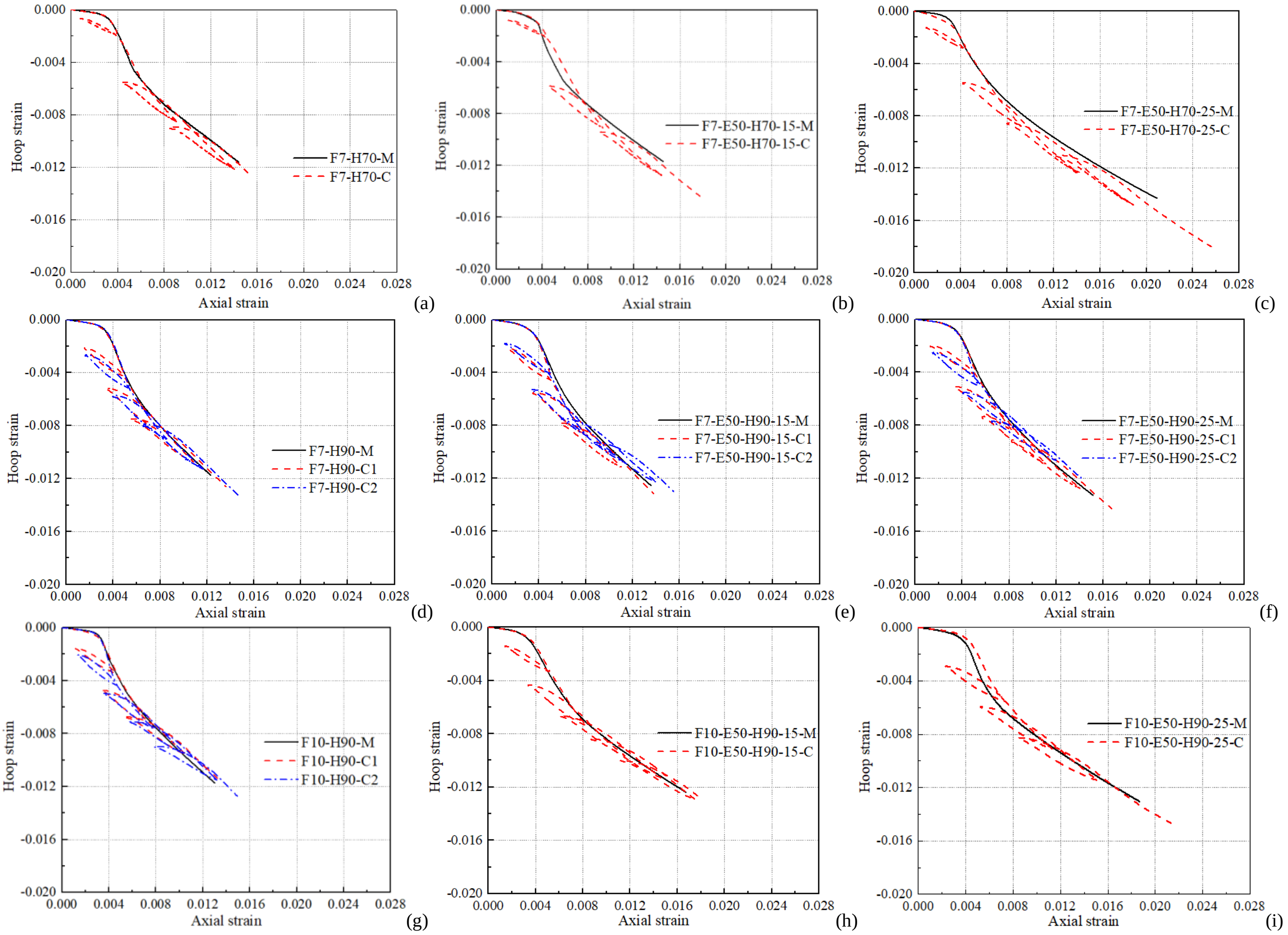

Fig. 7. Hoop strain-axial strain curves for tested specimens.

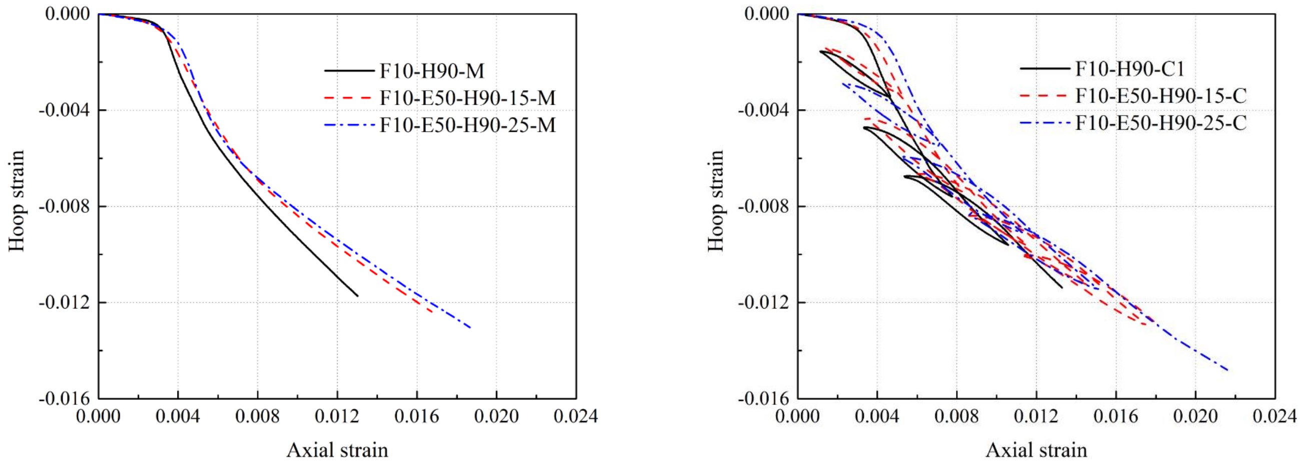

(a) Under monotonic loading (b) Under cyclic loading

Fig. 8. Comparisons of hoop strain-axial strain behavior between FRP-ECC-HSC composite columns and FRP-confined HSC columns.

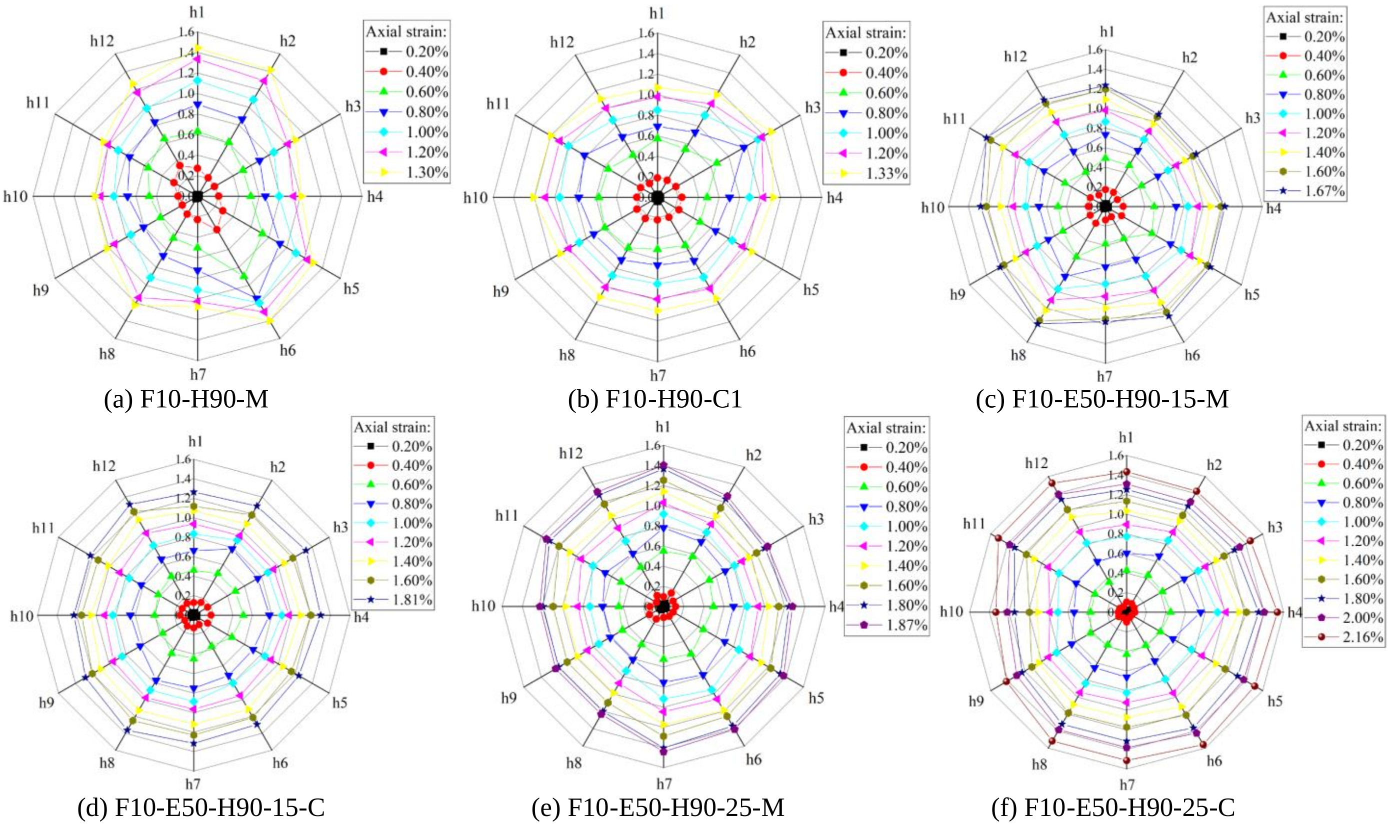

(a) F10-H90-M (b) F10-H90-C1 (c) F10-E50-H90-15-M

(d) F10-E50-H90-15-C (e) F10-E50-H90-25-M (f) F10-E50-H90-25-C

Fig. 9. Typical hoop strain distribution behavior of tested specimens.

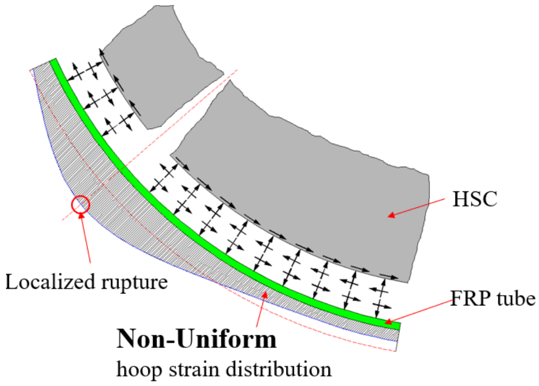

(a) FRP-confined HSC column

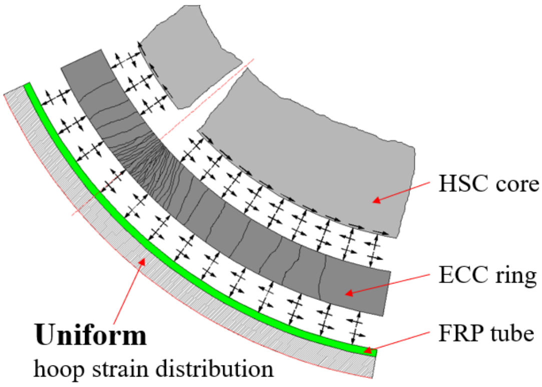

(b) FRP-ECC-HSC composite column

Fig. 10. Hoop strain distribution mechanism.

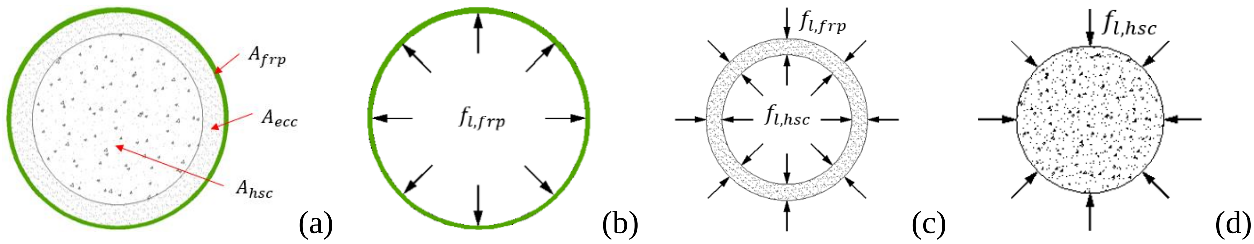

Fig. 11. Mechanical diagram of FRP-ECC-HSC composite column: (a) cross section; (b) FRP tube; (c) ECC ring; (d) HSC core.

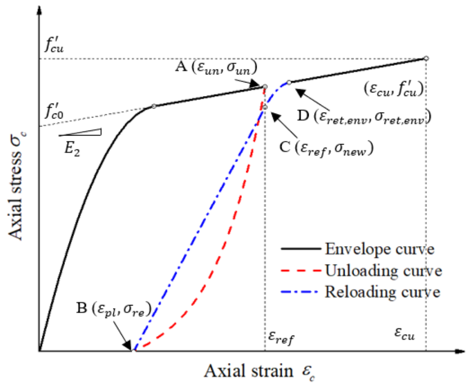

Fig. 12. Cyclic stress-strain model and key parameters.

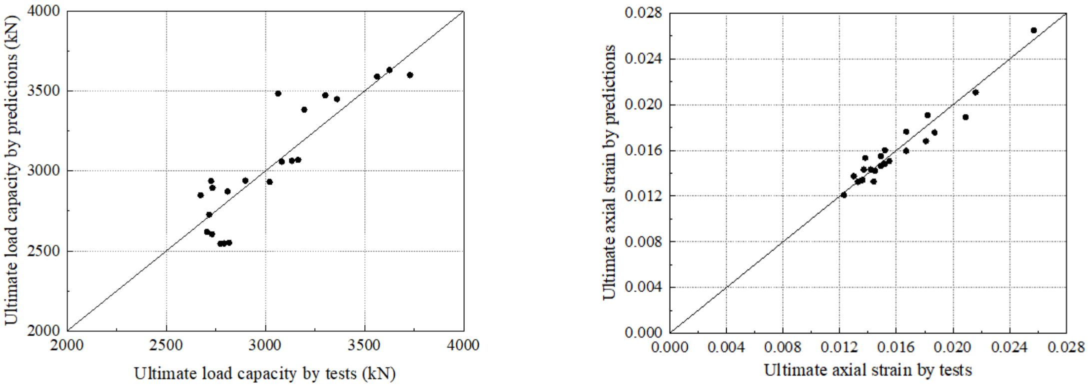

(a) Ultimate load capacity (b) Ultimate axial strain

Fig. 13. Predictions on ultimate conditions by the proposed equations.

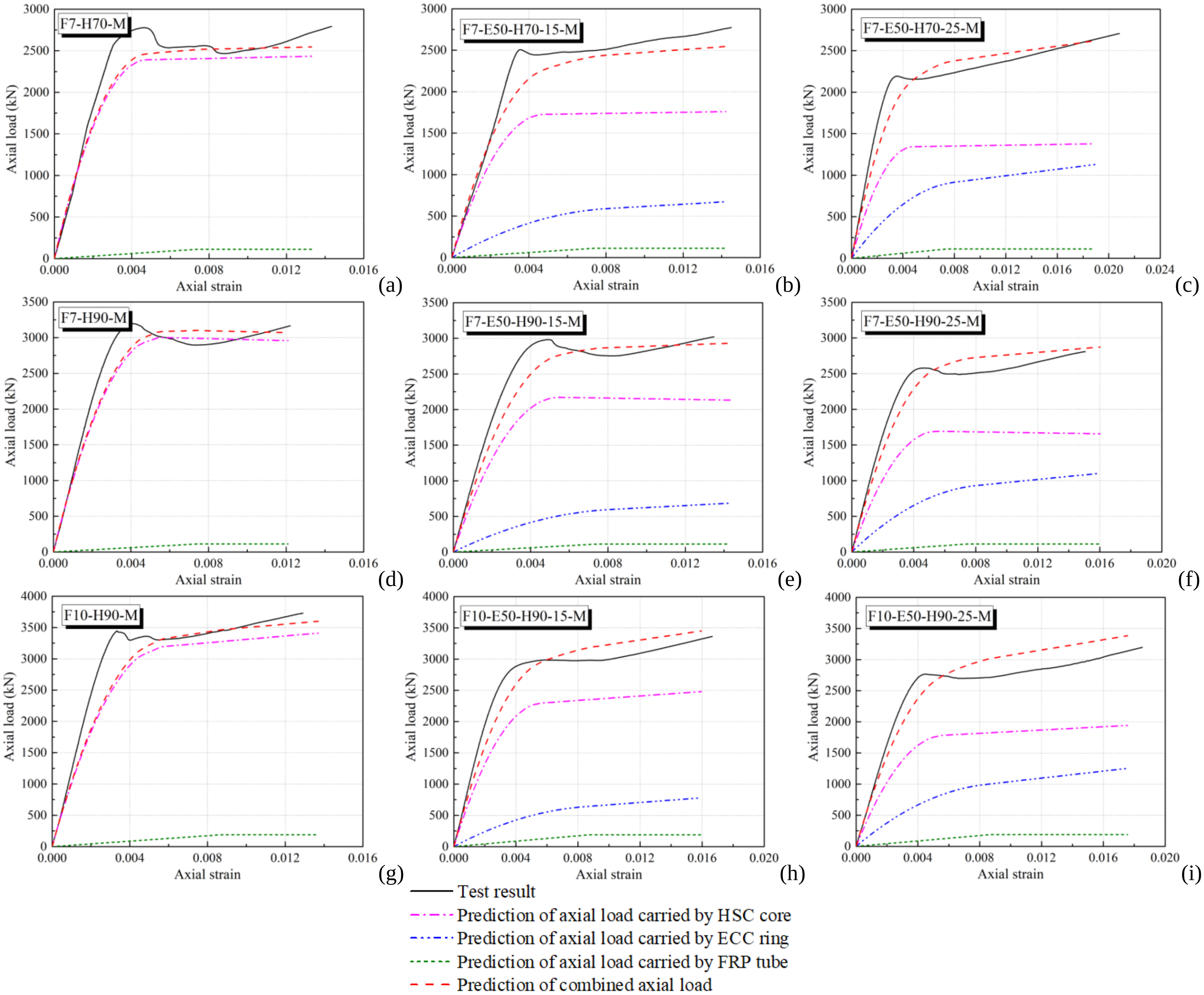

Fig. 14. Predictions of axial load-axial strain curves using the proposed monotonic stress-strain models.

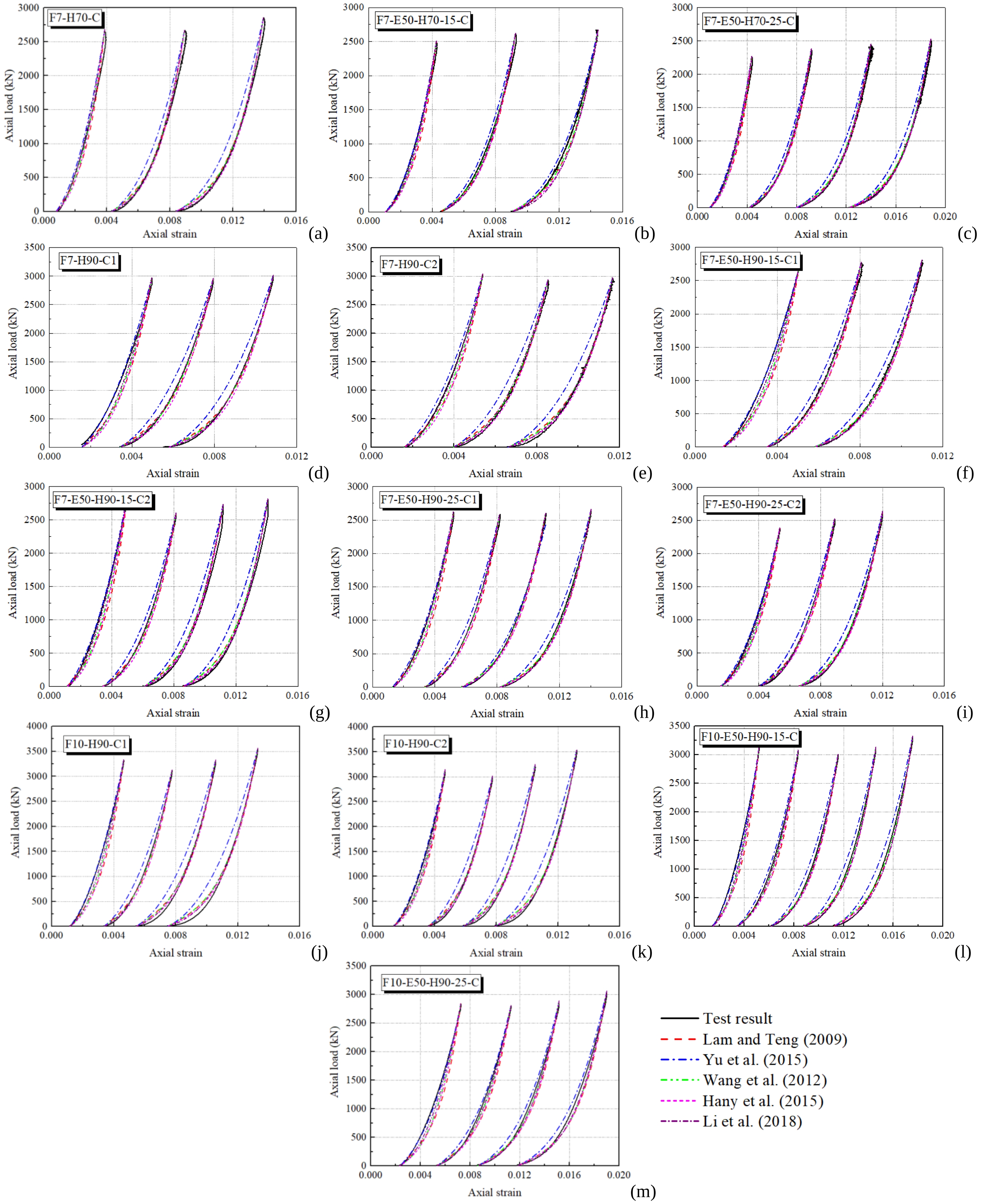

Fig. 15. Comparisons of unloading paths between test results and predictions by existing unloading models.

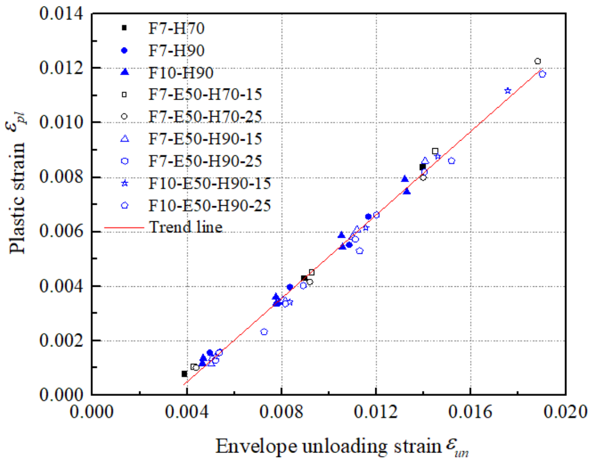

Fig. 16. Plastic strains for different unloading strains.

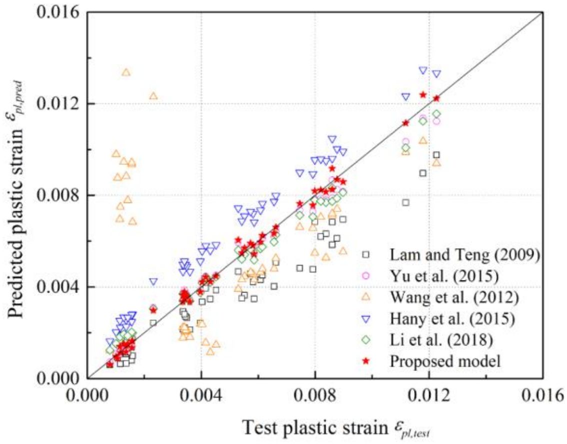

$\varepsilon_{pl,test}/\varepsilon_{pl,pred}$:

Models	Mean	CoV
Lam and Teng (2009)	1.37	0.178
Yu et al. (2015)	0.98	0.092
Wang et al. (2012)	1.18	0.658
Hany et al. (2015)	0.73	0.188
Li et al. (2018)	0.95	0.155
Proposed model	1.00	0.089

Fig. 17. Predicted plastic strains by different models.

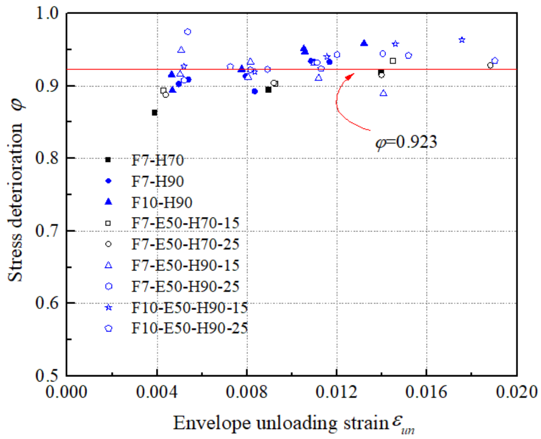

Fig. 18. Stress deterioration ratios for different unloading strains.

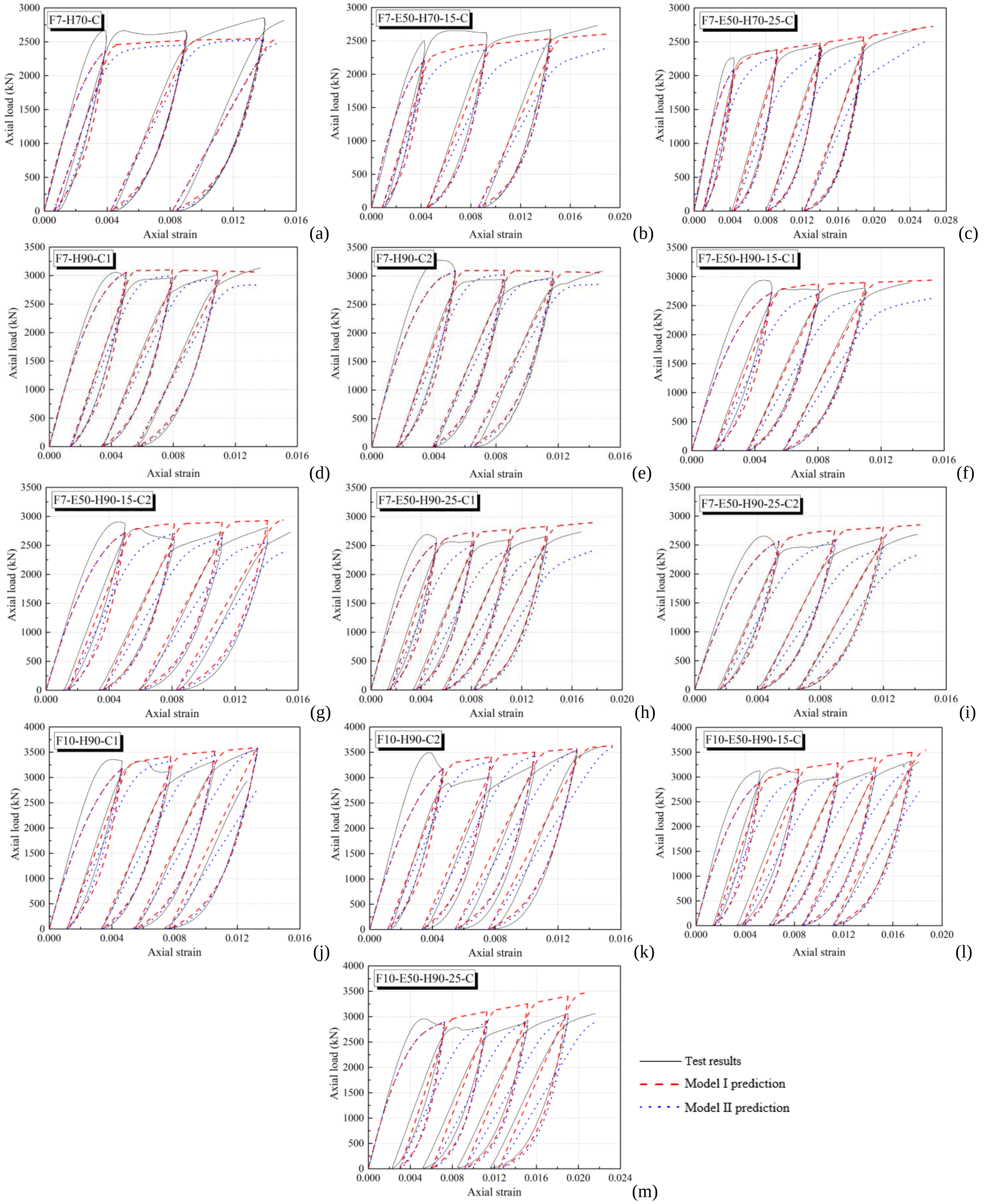

Fig. 19. Comparisons of cyclic axial load-axial curves between test results and model predictions.